



# ASTRO-H Space X-ray Observatory White Paper

Broad-band Spectroscopy and Polarimetry

P. Coppi (Yale University), Ł. Stawarz (JAXA), C. Done (Durham University),  
Y. Fukazawa (Hiroshima University), P. Gandhi (Durham University<sup>1</sup>), K. Hagino (JAXA),  
S. LaMassa (Yale University), P. Laurent (CEA Saclay), G. Madejski (KIPAC/SLAC)  
T. Mizuno (Hiroshima University), K. Mukai (NASA/GSFC/CRESST & UMBC), H. Odaka (JAXA),  
H. Tajima (Nagoya University), Y. Tanaka (Hiroshima University), F. Tombesi (University of Maryland), and  
M. Urry (Yale University)  
on behalf of the ASTRO-H Science Working Group

## Abstract

The broad energy range spanned by *ASTRO-H* instruments, from  $\sim 0.3$  to 600 keV, with its high spectral resolution calorimeter and sensitive hard X-ray imaging, offers unique opportunities to study black holes and their environments. The ability to measure polarization is particularly novel, with potential sources including blazars, Galactic pulsars and X-ray binaries. In this White Paper, we present an overview of the synergistic instrumental capabilities and the improvements over prior missions. We also show how *ASTRO-H* fits into the multi-wavelength landscape. We present in more detail examples and simulations of key science *ASTRO-H* can achieve in a typical 100 ksec observation when data from all four instruments are combined. Specifically, we consider observations of black-hole source (Cyg X-1 and GRS 1915+105), blazars (Mrk 421 and Mrk 501), a quasar (3C 273), radio galaxies (Centaurus A and 3C 120), and active galaxies with a strong starburst (Circinus and NGC 4945). We will also address possible new discoveries expected from *ASTRO-H*.

---

<sup>1</sup>Also at University of Southampton

## Complete list of the ASTRO-H Science Working Group

Tadayuki Takahashi<sup>a</sup>, Kazuhisa Mitsuda<sup>a</sup>, Richard Kelley<sup>b</sup>, Felix Aharonian<sup>c</sup>, Hiroki Akamatsu<sup>d</sup>, Fumie Akimoto<sup>e</sup>, Steve Allen<sup>f</sup>, Naohisa Anabuki<sup>g</sup>, Lorella Angelini<sup>b</sup>, Keith Arnaud<sup>b</sup>, Marc Audard<sup>i</sup>, Hisamitsu Awaki<sup>j</sup>, Aya Bamba<sup>k</sup>, Marshall Bautz<sup>l</sup>, Roger Blandford<sup>f</sup>, Laura Brenneman<sup>b</sup>, Greg Brown<sup>m</sup>, Edward Cackett<sup>n</sup>, Maria Chernyakova<sup>c</sup>, Meng Chiao<sup>b</sup>, Paolo Coppi<sup>o</sup>, Elisa Costantini<sup>d</sup>, Jelle de Plaa<sup>d</sup>, Jan-Willem den Herder<sup>d</sup>, Chris Done<sup>p</sup>, Tadayasu Dotani<sup>a</sup>, Ken Ebisawa<sup>a</sup>, Megan Eckart<sup>b</sup>, Teruaki Enoto<sup>q</sup>, Yuichiro Ezoe<sup>r</sup>, Andrew Fabian<sup>n</sup>, Carlo Ferrigno<sup>i</sup>, Adam Foster<sup>s</sup>, Ryuichi Fujimoto<sup>l</sup>, Yasushi Fukazawa<sup>u</sup>, Stefan Funk<sup>f</sup>, Akihiro Furuzawa<sup>e</sup>, Massimiliano Galeazzi<sup>v</sup>, Luigi Gallo<sup>w</sup>, Poshak Gandhi<sup>p</sup>, Matteo Guainazzi<sup>x</sup>, Yoshito Haba<sup>y</sup>, Kenji Hamaguchi<sup>h</sup>, Isamu Hatsukade<sup>z</sup>, Takayuki Hayashi<sup>a</sup>, Katsuhiro Hayashi<sup>a</sup>, Kiyoshi Hayashida<sup>g</sup>, Junko Hiraga<sup>aa</sup>, Ann Hornschemeier<sup>b</sup>, Akio Hoshino<sup>ab</sup>, John Hughes<sup>ac</sup>, Una Hwang<sup>ad</sup>, Ryo Iizuka<sup>a</sup>, Yoshiyuki Inoue<sup>a</sup>, Hajime Inoue<sup>a</sup>, Kazunori Ishibashi<sup>e</sup>, Manabu Ishida<sup>a</sup>, Kumi Ishikawa<sup>q</sup>, Yoshitaka Ishisaki<sup>f</sup>, Masayuki Ito<sup>ae</sup>, Naoko Iyomoto<sup>af</sup>, Jelle Kaastra<sup>d</sup>, Timothy Kallman<sup>b</sup>, Tuneyoshi Kamae<sup>f</sup>, Jun Kataoka<sup>ag</sup>, Satoru Katsuda<sup>a</sup>, Junichiro Katsuta<sup>u</sup>, Madoka Kawaharada<sup>a</sup>, Nobuyuki Kawai<sup>ah</sup>, Dmitry Khangulyan<sup>a</sup>, Caroline Kilbourne<sup>b</sup>, Masashi Kimura<sup>ai</sup>, Shunji Kitamoto<sup>ab</sup>, Tetsu Kitayama<sup>aj</sup>, Takayoshi Kohmura<sup>ak</sup>, Motohide Kokubun<sup>a</sup>, Saori Konami<sup>r</sup>, Katsuji Koyama<sup>al</sup>, Hans Krimm<sup>b</sup>, Aya Kubota<sup>am</sup>, Hideyo Kunieda<sup>e</sup>, Stephanie LaMassa<sup>o</sup>, Philippe Laurent<sup>an</sup>, François Lebrun<sup>an</sup>, Maurice Leutenegger<sup>b</sup>, Olivier Limousin<sup>an</sup>, Michael Loewenstein<sup>b</sup>, Knox Long<sup>ao</sup>, David Lumb<sup>ap</sup>, Grzegorz Madejski<sup>f</sup>, Yoshitomo Maeda<sup>a</sup>, Kazuo Makishima<sup>aa</sup>, Maxim Markevitch<sup>b</sup>, Hironori Matsumoto<sup>e</sup>, Kyoko Matsushita<sup>aq</sup>, Dan McCammon<sup>ar</sup>, Brian McNamara<sup>as</sup>, Jon Miller<sup>at</sup>, Eric Miller<sup>l</sup>, Shin Mineshige<sup>au</sup>, Ikuyuki Mitsuishi<sup>e</sup>, Takuya Miyazawa<sup>e</sup>, Tsunefumi Mizuno<sup>u</sup>, Koji Mori<sup>z</sup>, Hideyuki Mori<sup>e</sup>, Koji Mukai<sup>b</sup>, Hiroshi Murakami<sup>av</sup>, Toshio Murakami<sup>t</sup>, Richard Mushotzky<sup>h</sup>, Ryo Nagino<sup>g</sup>, Takao Nakagawa<sup>a</sup>, Hiroshi Nakajima<sup>g</sup>, Takeshi Nakamori<sup>aw</sup>, Shinya Nakashima<sup>a</sup>, Kazuhiro Nakazawa<sup>aa</sup>, Masayoshi Nobukawa<sup>al</sup>, Hirofumi Noda<sup>q</sup>, Masaharu Nomachi<sup>ax</sup>, Steve O' Dell<sup>ay</sup>, Hirokazu Odaka<sup>a</sup>, Takaya Ohashi<sup>r</sup>, Masanori Ohno<sup>u</sup>, Takashi Okajima<sup>b</sup>, Naomi Ota<sup>az</sup>, Masanobu Ozaki<sup>a</sup>, Frits Paerels<sup>ba</sup>, Stéphane Paltani<sup>i</sup>, Arvind Parmar<sup>x</sup>, Robert Petre<sup>b</sup>, Ciro Pinto<sup>n</sup>, Martin Pohl<sup>i</sup>, F. Scott Porter<sup>b</sup>, Katja Pottschmidt<sup>b</sup>, Brian Ramsey<sup>ay</sup>, Rubens Reis<sup>at</sup>, Christopher Reynolds<sup>h</sup>, Claudio Ricci<sup>au</sup>, Helen Russell<sup>n</sup>, Samar Safi-Harb<sup>bb</sup>, Shinya Saito<sup>a</sup>, Hiroaki Sameshima<sup>a</sup>, Goro Sato<sup>ag</sup>, Kosuke Sato<sup>aq</sup>, Rie Sato<sup>a</sup>, Makoto Sawada<sup>k</sup>, Peter Serlemitsos<sup>b</sup>, Hiromi Seta<sup>bc</sup>, Aurora Simionescu<sup>a</sup>, Randall Smith<sup>s</sup>, Yang Soong<sup>b</sup>, Łukasz Stawarz<sup>a</sup>, Yasuharu Sugawara<sup>bd</sup>, Satoshi Sugita<sup>j</sup>, Andrew Szymkowiak<sup>o</sup>, Hiroyasu Tajima<sup>e</sup>, Hiromitsu Takahashi<sup>u</sup>, Hiroaki Takahashi<sup>g</sup>, Yoh Takei<sup>a</sup>, Toru Tamagawa<sup>q</sup>, Takayuki Tamura<sup>a</sup>, Keisuke Tamura<sup>e</sup>, Takaaki Tanaka<sup>al</sup>, Yasuo Tanaka<sup>a</sup>, Yasuyuki Tanaka<sup>u</sup>, Makoto Tashiro<sup>bc</sup>, Yuzuru Tawara<sup>e</sup>, Yukikatsu Terada<sup>bc</sup>, Yuichi Terashima<sup>j</sup>, Francesco Tombesi<sup>b</sup>, Hiroshi Tomida<sup>ai</sup>, Yohko Tsuboi<sup>bd</sup>, Masahiro Tsujimoto<sup>a</sup>, Hiroshi Tsunemi<sup>g</sup>, Takeshi Tsuru<sup>al</sup>, Hiroyuki Uchida<sup>al</sup>, Yasunobu Uchiyama<sup>ab</sup>, Hideki Uchiyama<sup>be</sup>, Yoshihiro Ueda<sup>au</sup>, Shutaro Ueda<sup>g</sup>, Shiro Ueno<sup>ai</sup>, Shinichiro Uno<sup>bf</sup>, Meg Urry<sup>o</sup>, Eugenio Ursino<sup>v</sup>, Cor de Vries<sup>d</sup>, Shin Watanabe<sup>a</sup>, Norbert Werner<sup>f</sup>, Dan Wilkins<sup>w</sup>, Shinya Yamada<sup>r</sup>, Hiroya Yamaguchi<sup>b</sup>, Kazutaka Yamaoka<sup>e</sup>, Noriko Yamasaki<sup>a</sup>, Makoto Yamauchi<sup>z</sup>, Shigeo Yamauchi<sup>az</sup>, Tahir Yaqoob<sup>b</sup>, Yoichi Yatsu<sup>ah</sup>, Daisuke Yonetoku<sup>t</sup>, Atsumasa Yoshida<sup>k</sup>, Takayuki Yuasa<sup>q</sup>, Irina Zhuravleva<sup>f</sup>, Abderahmen Zoghbi<sup>h</sup>, and John ZuHone<sup>b</sup>

<sup>a</sup>Institute of Space and Astronautical Science (ISAS), Japan Aerospace Exploration Agency (JAXA), Kanagawa 252-5210, Japan

<sup>b</sup>NASA/Goddard Space Flight Center, MD 20771, USA

<sup>c</sup>Astronomy and Astrophysics Section, Dublin Institute for Advanced Studies, Dublin 2, Ireland

<sup>d</sup>SRON Netherlands Institute for Space Research, Utrecht, The Netherlands

<sup>e</sup>Department of Physics, Nagoya University, Aichi 338-8570, Japan

<sup>f</sup>Kavli Institute for Particle Astrophysics and Cosmology, Stanford University, CA 94305, USA

<sup>g</sup>Department of Earth and Space Science, Osaka University, Osaka 560-0043, Japan

<sup>h</sup>Department of Astronomy, University of Maryland, MD 20742, USA

<sup>i</sup>Université de Genève, Genève 4, Switzerland

<sup>j</sup>Department of Physics, Ehime University, Ehime 790-8577, Japan

<sup>k</sup>Department of Physics and Mathematics, Aoyama Gakuin University, Kanagawa 229-8558, Japan

<sup>l</sup>Kavli Institute for Astrophysics and Space Research, Massachusetts Institute of Technology, MA 02139, USA

<sup>m</sup>Lawrence Livermore National Laboratory, CA 94550, USA

<sup>n</sup>Institute of Astronomy, Cambridge University, CB3 0HA, UK

<sup>o</sup>Yale Center for Astronomy and Astrophysics, Yale University, CT 06520-8121, USA

<sup>p</sup>Department of Physics, University of Durham, DH1 3LE, UK

<sup>q</sup>RIKEN, Saitama 351-0198, Japan

<sup>r</sup>Department of Physics, Tokyo Metropolitan University, Tokyo 192-0397, Japan

<sup>s</sup>Harvard-Smithsonian Center for Astrophysics, MA 02138, USA

- <sup>t</sup>Faculty of Mathematics and Physics, Kanazawa University, Ishikawa 920-1192, Japan
- <sup>u</sup>Department of Physical Science, Hiroshima University, Hiroshima 739-8526, Japan
- <sup>v</sup>Physics Department, University of Miami, FL 33124, USA
- <sup>w</sup>Department of Astronomy and Physics, Saint Mary's University, Nova Scotia B3H 3C3, Canada
- <sup>x</sup>European Space Agency (ESA), European Space Astronomy Centre (ESAC), Madrid, Spain
- <sup>y</sup>Department of Physics and Astronomy, Aichi University of Education, Aichi 448-8543, Japan
- <sup>z</sup>Department of Applied Physics, University of Miyazaki, Miyazaki 889-2192, Japan
- <sup>aa</sup>Department of Physics, University of Tokyo, Tokyo 113-0033, Japan
- <sup>ab</sup>Department of Physics, Rikkyo University, Tokyo 171-8501, Japan
- <sup>ac</sup>Department of Physics and Astronomy, Rutgers University, NJ 08854-8019, USA
- <sup>ad</sup>Department of Physics and Astronomy, Johns Hopkins University, MD 21218, USA
- <sup>ae</sup>Faculty of Human Development, Kobe University, Hyogo 657-8501, Japan
- <sup>af</sup>Kyushu University, Fukuoka 819-0395, Japan
- <sup>ag</sup>Research Institute for Science and Engineering, Waseda University, Tokyo 169-8555, Japan
- <sup>ah</sup>Department of Physics, Tokyo Institute of Technology, Tokyo 152-8551, Japan
- <sup>ai</sup>Tsukuba Space Center (TKSC), Japan Aerospace Exploration Agency (JAXA), Ibaraki 305-8505, Japan
- <sup>aj</sup>Department of Physics, Toho University, Chiba 274-8510, Japan
- <sup>ak</sup>Department of Physics, Tokyo University of Science, Chiba 278-8510, Japan
- <sup>al</sup>Department of Physics, Kyoto University, Kyoto 606-8502, Japan
- <sup>am</sup>Department of Electronic Information Systems, Shibaura Institute of Technology, Saitama 337-8570, Japan
- <sup>an</sup>IRFU/Service d'Astrophysique, CEA Saclay, 91191 Gif-sur-Yvette Cedex, France
- <sup>ao</sup>Space Telescope Science Institute, MD 21218, USA
- <sup>ap</sup>European Space Agency (ESA), European Space Research and Technology Centre (ESTEC), 2200 AG Noordwijk, The Netherlands
- <sup>aq</sup>Department of Physics, Tokyo University of Science, Tokyo 162-8601, Japan
- <sup>ar</sup>Department of Physics, University of Wisconsin, WI 53706, USA
- <sup>as</sup>University of Waterloo, Ontario N2L 3G1, Canada
- <sup>at</sup>Department of Astronomy, University of Michigan, MI 48109, USA
- <sup>au</sup>Department of Astronomy, Kyoto University, Kyoto 606-8502, Japan
- <sup>av</sup>Department of Information Science, Faculty of Liberal Arts, Tohoku Gakuin University, Miyagi 981-3193, Japan
- <sup>aw</sup>Department of Physics, Faculty of Science, Yamagata University, Yamagata 990-8560, Japan
- <sup>ax</sup>Laboratory of Nuclear Studies, Osaka University, Osaka 560-0043, Japan
- <sup>ay</sup>NASA/Marshall Space Flight Center, AL 35812, USA
- <sup>az</sup>Department of Physics, Faculty of Science, Nara Women's University, Nara 630-8506, Japan
- <sup>ba</sup>Department of Astronomy, Columbia University, NY 10027, USA
- <sup>bb</sup>Department of Physics and Astronomy, University of Manitoba, MB R3T 2N2, Canada
- <sup>bc</sup>Department of Physics, Saitama University, Saitama 338-8570, Japan
- <sup>bd</sup>Department of Physics, Chuo University, Tokyo 112-8551, Japan
- <sup>be</sup>Science Education, Faculty of Education, Shizuoka University, Shizuoka 422-8529, Japan
- <sup>bf</sup>Faculty of Social and Information Sciences, Nihon Fukushi University, Aichi 475-0012, Japan

# Contents

<b>1</b>	<b>Introduction</b>	<b>5</b>
<b>2</b>	<b>X-ray Polarimetry of Astrophysical Sources</b>	<b>6</b>
2.1	X-ray Polarimetry with SGD . . . . .	7
2.2	Crab Pulsar and Nebula . . . . .	8
2.3	Microquasars . . . . .	9
2.4	Blazars . . . . .	11
<b>3</b>	<b>Jet-Disk Coupling in Active Galaxies</b>	<b>13</b>
3.1	Quasar 3C 273 . . . . .	13
3.2	Radio Galaxy Centaurus A . . . . .	15
3.3	UFOs and Radio-Loud AGN . . . . .	16
<b>4</b>	<b>Starburst-AGN Connection in Nearby Galaxies</b>	<b>18</b>
4.1	Circinus Galaxy . . . . .	18
4.2	NGC 4945 . . . . .	20
<b>5</b>	<b>A Space for New Discoveries with <i>ASTRO-H</i></b>	<b>25</b>
5.1	Tidal Disruption Events . . . . .	25
5.2	High-redshift Blazars . . . . .	26
5.3	Non-thermal Emission of Novae . . . . .	28
5.4	Unidentified Hard X-ray/soft $\gamma$ -ray Sources . . . . .	28

# 1 Introduction

Any comprehensive insight into the nature of astrophysical sources of high-energy radiation and particles requires a *multi-wavelength* approach. That is because the high-temperature and non-thermal particles energized in extreme astrophysical environments emit over an extremely broad range of the electromagnetic spectrum, from the low-frequency radio domain up to high and very high energy  $\gamma$ -rays. Hence, high quality, multi-wavelength data is required to access the source energetics and content, and to identify robustly the dominant particle acceleration and radiative processes involved. Many of these sources are highly variable, so these data need to be simultaneous, and repeated so as to sample different source activity levels. Only recently such a task has become feasible, due to the development of modern ground-based and space-borne instruments, ranging from high-resolution radio interferometers (EVLA, ALMA, soon SKA) up to sensitive  $\gamma$ -ray satellites (AGILE, *Fermi*-LAT) and Cherenkov Telescopes (H.E.S.S., MAGIC, VERITAS, soon also CTA). The general scope of this white paper is to discuss the X-ray domain as seen by *ASTRO-H* in this multiwavelength context. We argue in particular that the operation of the Hard X-ray Imager (HXI) and the Soft Gamma-ray Detector (SGD), in *synergy* and not in conflict with the operation of the Soft X-ray Spectrometer System (SXS), assures the sensitivity, energy resolution, and spectral coverage necessary for achieving a quantitative progress in the field (see also Takahashi et al., 2013).

One of the most pressing open problems in high-energy astrophysics which can be resolved, at least partly, by future *ASTRO-H* observations, is the exact coupling between the accretion processes fueling supermassive black holes (SMBHs) in active galactic nuclei (AGN), and their jet activity. While it is now widely accepted that extremely luminous, relativistic jets associated with *some* AGN are formed via an efficient extraction of the energy and angular momentum from the SMBH/accretion disk system (Begelman et al., 1984), several crucial aspects of jet formation process are still under debate, including the exact relation between disk state transitions and jet production efficiency, and the role of any external circum-nuclear medium in jet collimation. As discussed in § 3 below, the data gathered with *ASTRO-H* can provide valuable and novel input on these subjects, robustly disentangling the AGN jet, accretion disk, and disk wind radiative signatures in several targets via detailed spectroscopy and timing analysis, augmented by multi-wavelength correlation studies involving simultaneous radio and  $\gamma$ -ray observations. Analogous studies have been successfully conducted in the past for Galactic jet sources associated with X-ray binaries, but only rarely for AGN, mostly due to the fact that jetted (‘radio-loud’) AGN are much dimmer in X-rays than nearby XRBs. Thus, only with the new-generation X-ray telescopes such as *ASTRO-H* can the jet-accretion disk coupling in active galaxies be analyzed extensively enough to reach robust conclusions.

The other relevant topic calling for in-depth observational studies with *ASTRO-H* is the interplay between the SMBH activity and the nuclear starburst activity in evolving galaxies. There is general consensus that there is a strong connection between these processes, and that this link is crucial for understanding galaxy formation processes in general (see, e.g., Kormendy & Ho, 2013). However, previous investigations of the problem were hampered by the fact that available X-ray data with limited energy resolution and spectral coverage did not allow for a robust partition between the AGN and the starburst emission components in the observed spectra. As discussed in § 4, broad-band X-ray spectroscopy of even particularly complex and therefore particularly interesting systems simultaneously with SXS, HXI, and SGD, will enable address this issue properly.

The AGN-starburst connection and the jet-disk coupling in active galaxies are not the only topics of interest in the context of ‘broad-band’ studies with *ASTRO-H*, and in § 5 we briefly mention some other selected problems, focusing there on the potential of hard X-ray instruments HXI and SGD operating jointly in the 5 – 600 keV range. The hard X-ray/soft  $\gamma$ -ray astronomy *is* the field for making new discoveries indeed, simply because this electromagnetic window is the least studied one so far, due to severe instrumental limitations and challenges. The joint HXI and SGD observations are therefore very relevant for constraining poorly known properties of various types of astrophysical systems which release bulk of their radiative output around MeV photon energies, including  $\gamma$ -ray detected novae, high- $z$  blazars, or tidal disruption events. However, the particularly exciting and unique hallmark of *ASTRO-H* is the potential for the hard X-ray polarimetry with the SGD. This issue is discussed first in § 2 below.

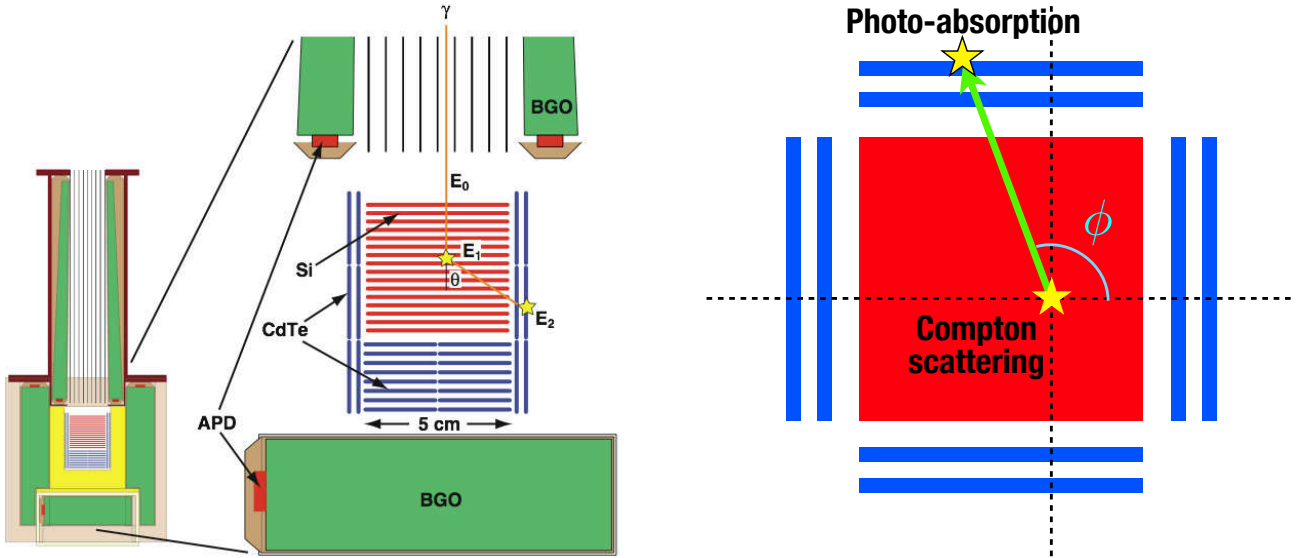


**Figure 1:** Schematic drawing of a single Compton camera unit of the SGD. The left panel shows a side view and the right panel presents the top view. The system measures two interactions (normally, Compton scattering and photo-absorption) and determines geometrical information on the scattering, namely the scattering angle  $\theta$  and the azimuth angle  $\phi$ .

## 2 X-ray Polarimetry of Astrophysical Sources

In addition to imaging, spectroscopy, and timing measurements, polarimetry in the X-ray and  $\gamma$ -ray bands is a new promising probe of high-energy phenomena in the Universe. In general, polarimetry provides us with crucial information about the radiation mechanisms involved, as well as the structure and content of the emitting regions. That is especially true in the X-ray domain, since polarization signatures in this range may arise from vastly different processes, including bremsstrahlung emission from anisotropic electron distribution, synchrotron emission in ordered magnetic fields, anisotropic Compton scattering, inverse-Comptonization of a polarized photon field, or finally, photon propagation through a highly magnetized plasma ( $B \geq 10^{12}$  G). Hence, substantially polarized X-ray emission may in principle be expected in a variety of astrophysical systems such as stellar flares, pulsars, pulsar nebulae, magnetars, accreting white dwarfs, supernova remnants, black hole accretion disks and coronae, jetted AGN, microquasars, or gamma-ray bursts (see Lei et al., 1997; Blandford et al., 2002; Bellazzini et al., 2010; Krawczynski et al., 2011, and also the “Pulsars & Magnetars” *ASTRO-H* White Paper).

The problem is, however, that X-ray polarization measurements are much more challenging compared with those at other wavelengths such as optical, infrared, or radio bands. The only satellite instruments with significant polarization capability were *OSO-8*, launched in 1975, which detected the Crab nebula (Weisskopf et al., 1976), and provided upper limits for several other X-ray bright Galactic sources at 2.6 and 5.2 keV, and *INTEGRAL* SPI and IBIS ((20 keV–1 MeV) which detected the Crab pulsar and nebulae (Dean et al., 2008; Forot et al., 2008), the gamma-ray burst GRB 041219 (McGlynn et al., 2007; Götz et al., 2009), and (marginally) the microquasar Cygnus X-1 (Laurent et al., 2011; Jourdain et al., 2012). However, these measurements suffer from large uncertainties due to low photon statistics and high in-orbit background. Similar issues apply to current balloon-borne X-ray polarimeters including PoGoLite (2–100 keV; Pearce et al., 2012), X-Calibur (20–80 keV; Beilicke et al., 2012), POLAR (50–500 keV; Orsi et al., 2011), and GRAPE (50–500 keV; Bloser et al., 2009). Nevertheless, the importance of polarimetry is recognised by the multiple proposals for new small satellite missions, such as POET (2–500 keV; Hill et al., 2008), GEMS (2–10 keV; Black et al., 2010), POLARIX (2–10 keV; Costa et al., 2010), or XIPE (2–10 keV; Soffitta et al., 2013), with SPHiNX (50–500 keV) and PolariS (2–80 keV) being selected for further study.

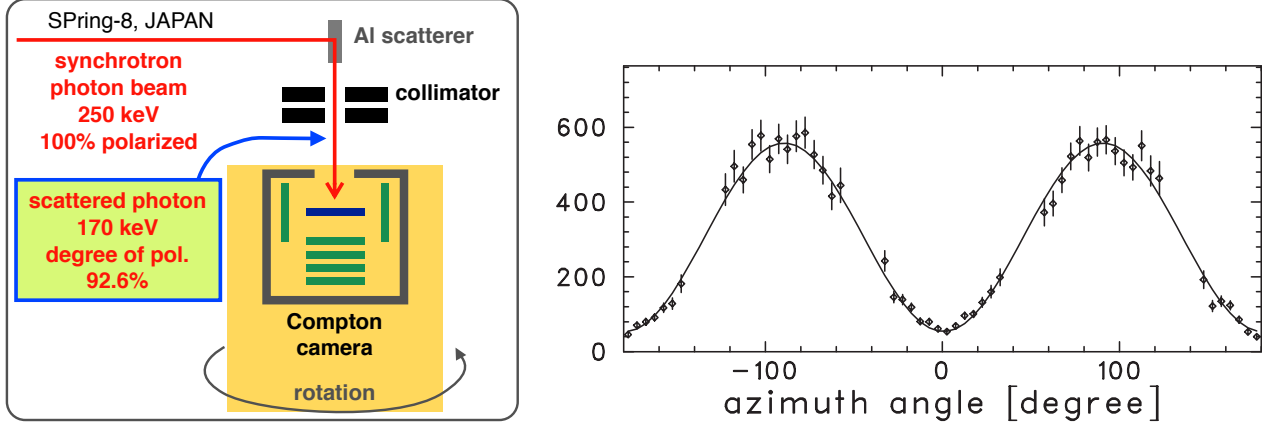


**Figure 2:** Left: the experimental setup of the polarization measurement at SPring-8. Synchrotron beam photons (250 keV) are scattered by an aluminum block and then collimated before incidence to the Compton camera. The camera system can be rotated upon the incident direction so that systematic uncertainties due to roll angle can be evaluated. Right: the obtained distribution of the azimuth angle after the response correction.

## 2.1 X-ray Polarimetry with SGD

The SGD is designed not only for spectroscopy but also for high-precision polarimetry by measuring Compton scattering in the detector system (Tajima et al., 2010a,b; Watanabe et al., 2012, 2014). Moreover, this instrument will be the first hard X-ray/soft  $\gamma$ -ray polarimeter in orbit that has moderate collection area and low instrumental background. For this reason, the SGD will improve the sensitivity and precision of polarization measurements even in a relatively short exposure time.<sup>1</sup> The SGD covers the energy range from about 50 keV up to 600 keV. The sensitivity peak is at 80–100 keV, depending on the signal brightness.

The polarization measurement by the SGD utilizes the anisotropy of the scattering direction of Compton scattering. As shown in Figure 1, the instrument determines the scattering process of an incident photon in the sensitive detectors by measuring the deposited energies and positions of the interactions. The differential cross section of Compton scattering is given by the Klein-Nishina formula,

$$\frac{d\sigma}{d\Omega} = \frac{r_e^2}{2} \left( \frac{E'}{E} \right) \left( \frac{E}{E'} + \frac{E'}{E} - 2 \sin^2 \theta \cos^2 \chi \right), \quad (1)$$

where  $r_e$  denotes the classical electron radius,  $\theta$  and  $\chi$  denote the scattering angle and the azimuth angle of scattering measured from the polarization angle, respectively, while  $E$  and  $E'$  are energies before and after the scattering:

$$E' = \frac{E}{1 + \frac{E}{m_e c^2} (1 - \cos \theta)}. \quad (2)$$

These formulae show that the azimuthal angle of Compton scattering has sinusoidal distribution, peaking at  $\pm 90^\circ$  to the polarization plane.

Takeda et al. (2010) demonstrated the capability of the SGD for high-precision polarimetry with a prototype model in the synchrotron photon beam at SPring-8, Japan. The left panel of Figure 2 shows the experimental setup, where the Compton camera measures the collimated 170 keV photons which are scattered by an aluminum block and have polarization fraction of 92.6%. To extract polarization information, the azimuthal angle distribution has to be corrected for the detector response, including both the detection efficiency and shielding by passive material. Monte Carlo simulations are used to quantify the effect of the complicated structure of the Compton camera system. The obtained distribution of azimuthal angle after the response correction, shown in

<sup>1</sup>Conventional instruments that use the principle of Compton polarimetry require longer exposure and nontrivial treatment of evaluating systematic uncertainties.

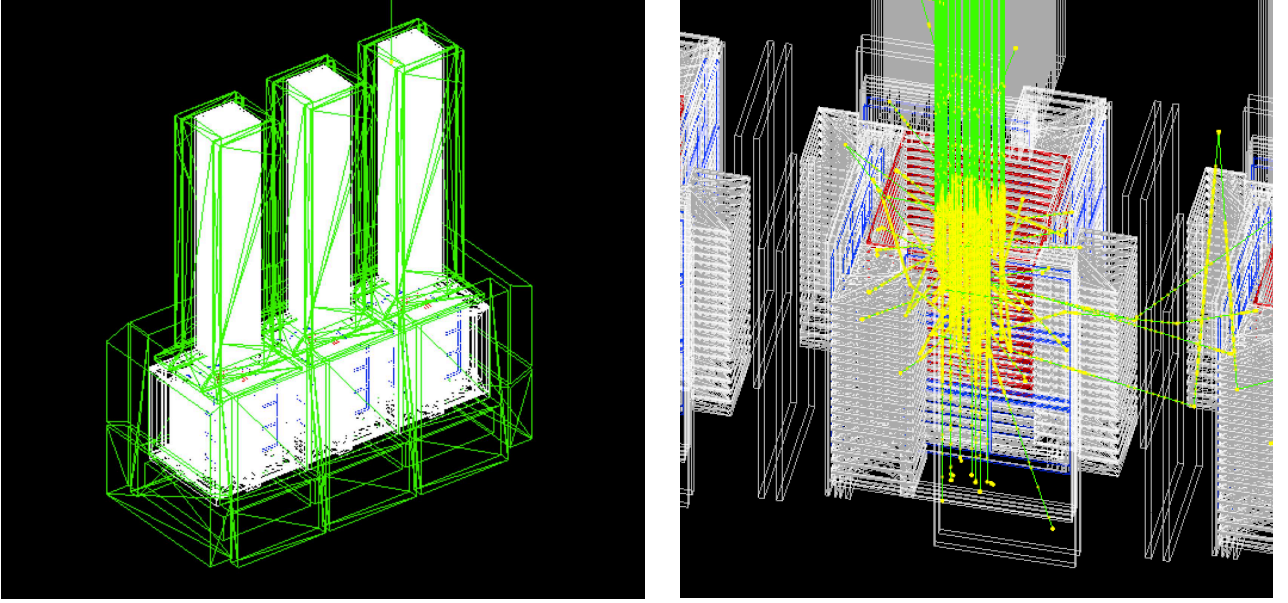


**Figure 3:** Mass model of the SGD for Monte Carlo simulations. Left: the whole SGD unit. Right: zoom up about one of the Compton cameras. In the right panel, photon trajectories are drawn as green lines and interactions are drawn in yellow.

the right panel of Figure 2. This gives a polarization fraction of  $91 \pm 1\%$  and polarization angle of  $0.2^\circ \pm 0.4^\circ$ , consistent with the input with small uncertainties.<sup>2</sup>

We have developed an SGD simulator using the Geant4 toolkit. This evaluates the detector response and estimates in-orbit background, so it can be used for optimizing observatory operations as well as data analysis (Odaka et al., 2010; Ozaki et al., 2012). Figure 3 shows the mass model of the SGD for the Monte Carlo simulations. This describes the geometry and material of the sensitive detectors and the surrounding passive structures. Physical processes taking place in the instrument are accurately tracked by the simulator, which also takes account of charge transport in semiconductor sensors, signal readout electronics and data acquisition system in order to reproduce the detector response. We use this simulator to assess the polarisation signal which can be detected against the background, including the additional polarised light produced from scattering within the detector and its housing. However, there are still systematic uncertainties due to uncertainties in the mass model and background. It is important to investigate these using both the simulations and on-ground calibration measurements. Further systematic uncertainties can be reduced by performing multiple observations with different roll angle of the spacecraft.

## 2.2 Crab Pulsar and Nebula

The Crab pulsar and nebula, as the X-ray and  $\gamma$ -ray brightest source in sky, is the most feasible target for the polarimetry with the SGD. Importantly, the pulsar and nebular emission components can be decomposed despite the pulsar being only  $\sim 10\%$  of the nebula flux as they have different spectral, timing and polarisation behaviour. These two components have different origins: the pulsar emits via curvature radiation in the pulsar magnetosphere while the pulsar wind nebula is dominated by the synchrotron radiation. The SGD has sufficient timing resolution ( $< 1$  ms) to resolve the behaviour on the pulsar spin period of 33 ms.

We conducted simulations to evaluate the technical feasibility of the SGD polarimetry. First, we show simulation results for the two SGD units for a 100 ks observation of the Crab nebula in Figure 4. The input spectrum is assumed to be a power law,  $F(E) = K \times E^{-\Gamma}$ , with the normalization  $K = 11.6 \text{ photons s}^{-1} \text{ cm}^{-2}$  at 1 keV, and the photon index  $\Gamma = 2.1$ . Assuming a polarization fraction of 50%, we expect clear detection of the polarization from a 1 Crab source. The fitted values are  $48 \pm 1\%$  for the polarization fraction and  $0.1^\circ \pm 0.5^\circ$  for

<sup>2</sup>All the errors in this section are presented in  $1\sigma$  values.



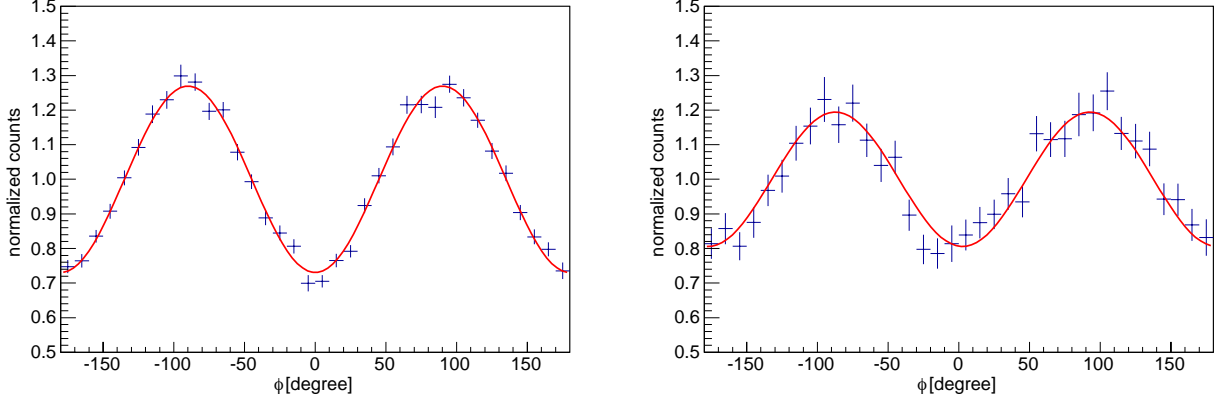


**Figure 4:** Simulated polarimetry results of 100 ks observation of Crab in energy bands of 60–100 keV (left) and 180–330 keV (right). Both assume flux of 1 Crab, photon index of 2.1, and polarization fraction of 50%. These azimuth angle distribution are corrected by the detector response for unpolarized radiation.

the polarization angle in the energy range of 60–100 keV. At the higher band between 180 keV and 330 keV, photon statistics becomes limited due to decreasing detection efficiency, but the result still reveals a significant detection; the fitted values are  $48 \pm 3\%$  for the polarization fraction and  $2.7^\circ \pm 1.6^\circ$  for the polarization angle. These agree well with the assumed values for the simulation (50% polarization and  $0^\circ$  angle). Moreover, the statistical uncertainty will be much smaller than observational uncertainties of currently reported measurements by *INTEGRAL* (Dean et al., 2008; Forot et al., 2008; Moran et al., 2013), though we need to be careful about systematic errors. On the other hand, in the case of Crab the polarization information in the non-peak phase can be used as a background in order to reduce the background systematics; as a result, the sensitivity to the Crab pulsar polarization can be better than for other sources with comparable brightness.

Moran et al. (2013) studied the linear polarization of the Crab Nebula and pulsar in both the optical (HST/ACS) and in the  $\gamma$ -rays (*INTEGRAL*/IBIS). For both wavelengths, they found evidence of an alignment between the polarization position angle of the pulsar and its rotation axis. They confirmed that the synchrotron knot (Hester et al., 1995) located  $0.65''$  SE of the pulsar is responsible for the highly polarized off-pulse emission seen in both the optical (Smith et al., 1988; Słowińska et al., 2009) and  $\gamma$ -rays (Forot et al., 2008). Hence, further multi-wavelength studies of this astrophysical system with *ASTRO-H* would enable a more precise check for any correlations between the two energy ranges. This could show whether the polarization of the system is linked to the highly variable flux from the nebula seen in the 100–300 MeV range by the *Fermi* and *AGILE* telescopes (Tavani et al., 2011; Striani et al., 2011; Mayer et al., 2013, and references therein) — the so-called  $\gamma$ -ray flares. Such monitoring could be achieved through simultaneous/joint observations using optical polarimeters such as the Galway Astronomical Stokes Polarimeter (GASP; Collins et al., 2013). These multi-wavelength studies will benefit from the good *ASTRO-H* timing capabilities, and will be nicely complemented by high time resolution optical polarimeters. This will enable detailed phase-resolved spectro-polarimetry analysis.

### 2.3 Microquasars

Jetted black hole XRBs, or ‘microquasars’, are the other promising targets for the X-ray polarimetry with the SGD, since the reflection at the accretion disk, thermal Comptonization in a hot disk corona, and also synchrotron emission of the jet electrons, can all lead to distinct polarization signatures in the hard X-ray/soft  $\gamma$ -ray bands. Hence, energy dependent polarization measurements (‘spectropolarimetry’) of such systems is in principle capable of constraining the geometry of their accretion flows, and the magnetic structure of their jets.

A marginal detection of soft X-ray polarization from Cygnus X-1 was reported by Long et al. (1980) with the position angle of  $162^\circ \pm 13^\circ$  at 2.6 keV. Assuming the disk origin of the soft X-ray polarization signal, and adopting a simplified model for such (with no relativistic effect taken into account), the position angle

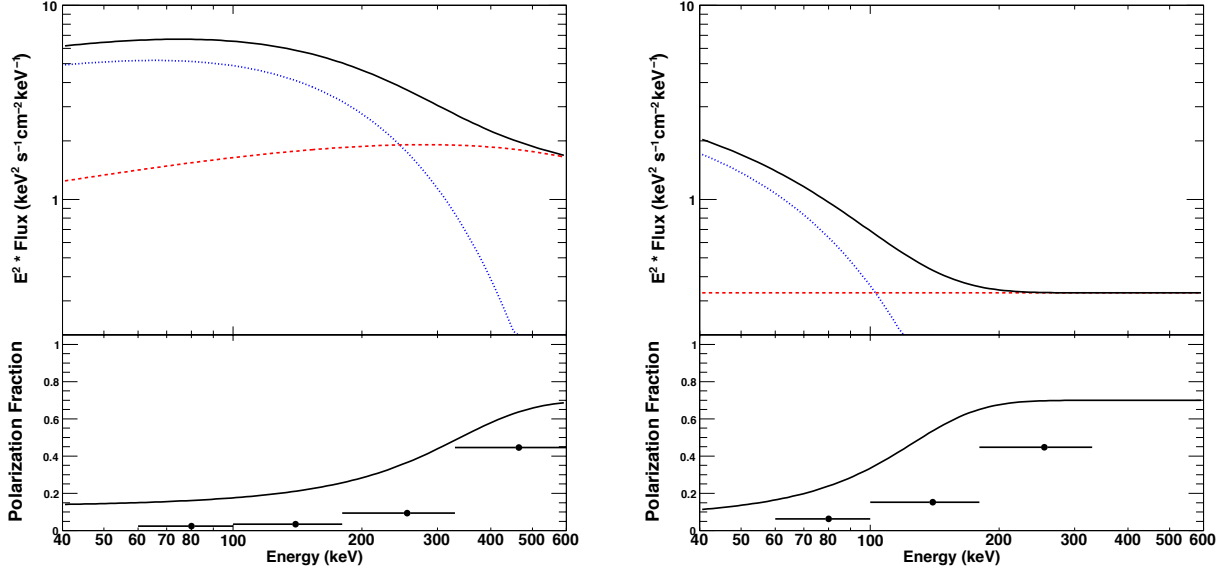


**Figure 5:** Left: Cygnus X-1 model spectrum (top panel) and the expected polarization fraction (bottom panel). In the top panel the low energy and high energy components are shown by blue and red curves, respectively. In the bottom panel the  $MDP_{99}$  is also plotted. Right: The same as the left panel but for GRS 1915+105.

of the polarization is expected to be parallel or perpendicular to the disk major axis depending on the disk state (Lightman & Shapiro, 1976); the value given by Long et al. (1980) is actually consistent with the jet position angle measured in the radio band (about  $-21^\circ$  to  $-24^\circ$ ; Stirling et al., 2001). More recently, Laurent et al. (2011) observed Cygnus X-1 with *INTEGRAL* IBIS and resolved two emission components in the 20 keV–2 MeV range. They reported that a second (high-energy) component exhibits a polarization above 400 keV with a polarization fraction of  $67\% \pm 33\%$ . Jourdain et al. (2012) utilized the *INTEGRAL* SPI and reinforced the finding by Laurent et al. (2011). They reported a polarization signal above 230 keV with a mean polarization fraction of  $76\% \pm 15\%$  and at a position angle of  $42^\circ \pm 3^\circ$ . Note that, as described in Jourdain et al. (2012), the correct position angle measured by Laurent et al. (2011) is not  $140^\circ$  but in fact  $180^\circ - 140^\circ = 40^\circ$ . All in all, the *INTEGRAL* spectropolarimetry suggests that the hard component, which dominates the flux above 100 keV, is due to the jet synchrotron emission. However, the surprisingly high polarization fraction and the apparent deviation of the position angle from the jet orientation (by about  $65^\circ$ ), make the interpretation quite problematic (see the discussion in Zdziarski et al., 2014). An independent and precise spectropolarimetry is necessary to deepen our understanding of high-energy emission from this important source, and the *ASTRO-H* SGD is an ideal instrument for this purpose.

In order to evaluate the SGD sensitivity for polarization measurements, we first modeled the Cygnus X-1  $\gamma$ -ray spectrum based on Jourdain et al. (2012). We represented their low-energy component (presumably Comptonization, expected to show little or no polarization) and a high-energy component (presumably highly polarized jet synchrotron emission) with  $F(E)_{\text{soft}} = 1.3 \times (E/\text{keV})^{-1.6} \times \exp[-(E/160 \text{ keV})^{1.4}] \text{ ph s}^{-1} \text{ cm}^{-2} \text{ keV}^{-1}$  and  $F(E)_{\text{hard}} = 0.3 \times (E/\text{keV})^{-1.6} \times \exp[-(E/700 \text{ keV})] \text{ ph s}^{-1} \text{ cm}^{-2} \text{ keV}^{-1}$ , respectively. We then evaluated the polarization sensitivity across four energy bands in the 60–600 keV range. The minimum detectable polarization at the 99% confidence level was calculated as

$$MDP_{99} = \frac{4.29}{M \times R_S} \sqrt{\frac{R_S + R_B}{T}}, \quad (3)$$

where  $M$  is the modulation factor of the instrument,  $T$  is the observation time, and  $R_S$  and  $R_B$  are the source and the background count rates, respectively (Weisskopf et al., 2009). Based on the high polarization fraction reported by *INTEGRAL* IBIS/SPI, we assumed that the polarization fraction is 70% for the high energy (jet)

component. The results of the calculation for 100 ks exposure are summarized in Figure 5 (left panel), indicating that such an observation with the SGD is able to derive interesting constraints on the energy-dependent polarization measurements of Cygnus X-1 in the 60–600 keV range.

GRS 1915+105 is another promising target for the hard X-ray/soft  $\gamma$ -ray polarimetry with the SGD. This source is known for superluminal jet ejections with bulk velocities of the outflowing matter exceeding 90% of the light speed (Mirabel & Rodríguez, 1994). Rodríguez et al. (2008) monitored the source with the *INTEGRAL* IBIS, *RXTE*, and the Ryle Telescope for two years, and observed a possible correlation of the radio flux and that of the hard power-law component, indicating the emission from the jet in hard X-rays. Droulans & Jourdain (2009) observed the source with the *INTEGRAL* SPI and performed a spectral analysis in soft  $\gamma$ -rays. They classified the data into two, the soft sample and the hard sample, and found that in both samples the spectrum is represented by a thermal Comptonization component and a high-energy power-law component. We approximate their hard sample spectrum with  $F(E)_{\text{soft}} = 4.4 \times (E/\text{keV})^{-2.1} \times \exp[-(E/60 \text{ keV})^{1.4}] \text{ ph s}^{-1} \text{ cm}^{-2} \text{ keV}^{-1}$  plus  $F(E)_{\text{hard}} = 0.33 \times (E/\text{keV})^{-2.0} \text{ ph s}^{-1} \text{ cm}^{-2} \text{ keV}^{-1}$ , and evaluated the polarization measurement feasibility as we did for Cygnus X-1. The results are summarized in Figure 5 (right panel), in which we assumed the polarization fraction of the hard (jet) component at the maximum level of 70%. As shown, the SGD is able to detect polarization up to 300 keV. Even if the polarization fraction is smaller (30% in the hard component), we can still detect polarization up to 180 keV. We therefore are able to robustly establish (or strongly constrain) the jet emission in hard X-ray/soft  $\gamma$ -rays in GRS 1915+105 for the first time.

## 2.4 Blazars

Jetted AGN observed at small angle to the line of sight are classified as blazars. Blazars can be divided further into Flat Spectrum Radio Quasars (FSRQs) and BL Lacertae Objects (BL Lacs) based on the emission line diagnostics and other characteristics of their broad-band spectra (Urry & Padovani, 1995). X-ray continua of some BL Lacs (and in particular of ‘high frequency-peaked BL Lacs’, hereafter HBLs) are dominated by the synchrotron emission of the highest-energy jet electrons, and hence a strong X-ray polarization may be expected in such sources up to the maximum level of 70% (e.g., Pacholczyk & Swihart, 1967).

Polarization of blazar synchrotron emission is now routinely detected at radio and optical frequencies, with the polarization degree and position angle depending on frequency and the activity level of a source; a variety of particularly interesting phenomena have recently been discovered at optical frequencies, consisting of prominent position angle swings (by  $\geq 180$  deg) and polarization degree changes (from 0% up to  $> 40\%$ ) apparently related to the overall source state (as evidenced by coinciding  $\gamma$ -ray flares, or ejections of superluminal radio components; see Marscher et al., 2008; Abdo et al., 2010b, and references therein). These new observations allowed for a novel insight into the internal structure and magnetic field topology of AGN jets, which are among the most widely debated open questions in the high-energy astrophysics.

The additional spectropolarimetry of bright blazar sources at X-ray frequencies will allow to constrain further the physics of relativistic jets in active galaxies. The problem is, however, that HBLs are relatively low-power and in addition distant objects, which are therefore much dimmer in X-rays (in their typical quiescence states) than Galactic XRBs or nearby radio-quiet AGN of the Seyfert class. In addition, the quiescence synchrotron continua of the brightest objects of this type, such as Mrk 421 and Mrk 501, display a prominent curvature at X-ray energies, with the differential energy flux decreasing rapidly with the increasing photon energy. Still, the SGD can detect at least some HBLs during their flaring states, such as the April 1997 outburst of Mrk 501 during which the flat-spectrum synchrotron component extended up to  $\geq 100$  keV photon energies, with the persistent (over several days) flux of about  $\sim 100$  mCrab (Pian et al., 1998, see Figure 6, left panel). Such flares, although rare, are not unusual, and much can be learned from those. For example, the 2006 flare of HBL PKS 2155–304 witnessed at very-high energy  $\gamma$ -rays by the H.E.S.S. telescope (Aharonian et al., 2007) has ignited a vigorous discussion in the community on the location of the dominant  $\gamma$ -ray emission site in blazar sources, and on the role of magnetic reconnection in accelerating jet particles (electrons) up to  $> \text{TeV}$  energies.

We have simulated the performance of SGD during the Mrk 501 flare resembling the historical 97’ outburst (in a similar manner as described in § 2.2). We have assumed a power-law spectrum with the energy flux density

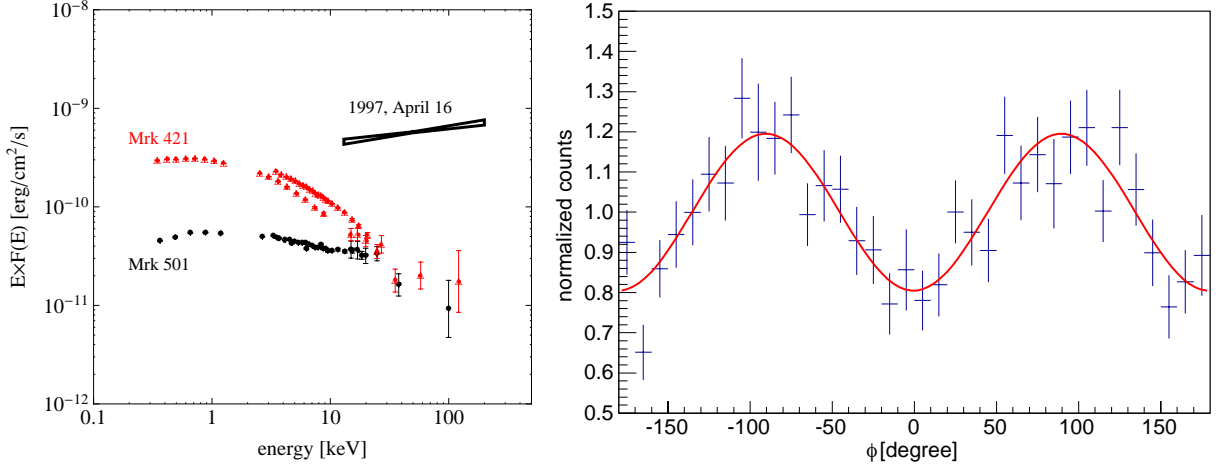


**Figure 6:** Left: Spectral energy distribution of the X-ray brightest HBLs, Mrk 421 and Mrk 501, during their quiescence (red triangles and black circles, from Abdo et al., 2011b,a, respectively), compared with the April 1997 flare of Mrk 501 (black bow-tie; from Pian et al., 1998). Right: Simulated polarimetry results of 100 ks SGD observation of Mrk 501 during the '97 outburst (energy band: 60–100 keV), assuming the energy flux density of  $F_{13-200\text{ keV}} = 15.9 \times 10^{-10} \text{ erg cm}^{-2} \text{ s}^{-1}$ , the photon index  $\Gamma = 1.84$ , and the 30% polarization degree.

of  $F_{13-200\text{ keV}} = 15.9 \times 10^{-10} \text{ erg cm}^{-2} \text{ s}^{-1}$  and the photon index  $\Gamma = 1.84$ ; the degree of polarization was taken conservatively as 30%. The azimuth angle distribution obtained in the simulation is shown in Figure 6 (right panel). In spite of the relatively conservative value for the polarization fraction, the simulation result shows clear modulation curve, yielding the polarization fraction of  $35.1 \pm 3.7\%$ , and the polarization angle of  $-0.4^\circ \pm 2.9^\circ$ . Thus hard X-ray polarimetry of blazars of the BL Lac types with SGD is therefore feasible, although restricted to the brightest outbursts. ToO observations of a flaring blazar should be therefore triggered by all-sky monitoring X-ray and  $\gamma$ -ray instruments (*Swift*-XRT and BAT, MAXI, *Fermi*-LAT and GBM), and joint with simultaneous radio and optical spectropolarimetry, in order to maximize the detection significance and the scientific gain.

Unlike in the case of low-power HBLs, the X-ray continua of luminous FSRQ are dominated by the inverse-Compton emission of the lowest-energy jet electrons (see Sikora et al., 2009). Importantly, this inverse-Compton emission can also be polarized at some level, with the polarization degree depending on polarization properties of soft target photons (jet synchrotron radiation, emission of the accretion disk and circumnuclear gas/dust external to the jet), on the scattering regime (Thomson vs. Klein-Nishina), and finally on the geometry of the emitting region and the jet bulk velocity (see Bonometto & Saggion, 1973; Begelman & Sikora, 1987; Celotti & Matt, 1994; Poutanen, 1994; McNamara et al., 2009; Krawczynski, 2012; Zhang & Boettcher, 2013). Model predictions are here still uncertain to some extent, but the emerging agreement is that the synchrotron self-Compton emission of blazar sources may be polarized up to even 40%. Interestingly, the X-ray continua of several bright FSRQs are expected to be dominated by the SSC emission. Hence, the SGD observations of such objects may in principle provide interesting constraints on the blazar emission models as well. The same is true also in the case of radio galaxies, which are believed to constitute the parent population of blazars, although the origin of the X-ray emission of even the brightest objects from this class is much more controversial, due to the expected significant, possibly even dominant, contribution from the accreting matter. The issue of disentangling the jet and disk emission components at X-ray photon energies is the subject of the following section.

It is important to comment here on the implications of a detected polarization from any extragalactic sources. Quantum gravity theories predict an energy-dependent photon velocity, and therefore a decrease of the polarization signal emitted by cosmologically distant objects. Currently, the positive detection of polarization from the Crab nebula provides the strongest limit in this respect, but any polarization detection of an *extragalactic* source will enable to revise this limit significantly (see, e.g., Maccione et al., 2008).

### 3 Jet-Disk Coupling in Active Galaxies

In non-blazar (‘misaligned’) radio-loud AGN, the observed X-ray spectra may contain a significant contribution, or even be dominated by the emission from the accretion disk and (more likely) the accretion disc coronae. The clearest evidence for this is the detection of a neutral, narrow Fe-K fluorescence lines in some systems (see Fukazawa et al., 2011a, 2014, and references therein). This line is produced by the accretion disc corona illuminating distant material (torus), and its presence in the spectrum means that the X-rays from the corona are not completely swamped by additional X-rays from the jet. Thus in these systems we can simultaneously see the accretion disk corona and the radio/ $\gamma$ -ray jet emission. Hence they constitute an exciting opportunity to investigate the jet-disk coupling, and therefore the jet launching processes, by means of a broad-band X-ray spectroscopy, hard X-ray/soft  $\gamma$ -ray polarimetry, and timing analysis joint with multiwavelength ( $\gamma$ -ray and high-resolution radio) observations of the selected bright targets. Yet such an analysis, analogous to what is routinely done for Galactic microquasars (see, e.g., Fender et al., 2009, and references therein), was hampered in the past by the fact that the corona and the jet X-ray emission components are not disentangled well in the majority of cases, with the exception of a few brightest objects.

Two broad line radio galaxies (BLRGs), namely 3C 111 and 3C 120, have been recently the subject of an extensive monitoring campaign to study the accretion disc-jet coupling (Marscher et al., 2002; Chatterjee et al., 2009, 2011). It was found that the major X-ray dips in the light curves are followed by ejections of bright superluminal knots in the radio jets of both targets. Assuming the dominant disk corona contribution at X-ray frequencies, these observations imply therefore a direct relation between the disk state transitions and the jet formation process in AGN. On the other hand, Tombesi et al. (2010b, 2012, 2013) presented a comparison of the parameters of the disk wind and the jet in radio galaxy 3C 111 on sub-pc scales. They found that the superluminal jet coexists with mildly relativistic outflows and that both of them are powerful enough to exert a concurrent feedback impact on their surrounding environment. Interestingly, there are several indications suggesting that the ultra-fast disk outflows in the studied systems might be placed within the ‘X-ray dips/radio outbursts’ cycle as well, providing the necessary pressure support for the efficient collimation and bulk acceleration of the electromagnetic jet freshly launched from the rotating SMBH/accretion disk system.

Clearly, *ASTRO-H* observations may enable a qualitative progress in understanding the jet-disk connection in AGN, as its performance (sensitivity, energy resolution, and energy range) will exceed that of the previously and currently available X-ray instruments. The particular targets discussed below in this context — the quasar 3C 273, low-power radio galaxy Centaurus A, and luminous broad-line radio galaxy 3C 120 — are all easily detectable with low- and high-energy instruments onboard the *ASTRO-H* in relatively short exposures, are often monitored with milli-arcsec radio interferometers, and are all the established  $\gamma$ -ray emitters. Hence, while the SXS will constrain precisely the emission and absorption lines in the soft band in those sources, thus providing a unique insight into the accretion processes, the HXI and SGD will characterize with unprecedented detail the spectral variability of the targets in the medium and hard bands, which may be next correlated with the extensive *Fermi*-LAT monitoring at  $\gamma$ -rays, along with the high-resolution radio data.

#### 3.1 Quasar 3C 273

3C 273 (redshift  $z = 0.158$ ) is one of the first quasars ever discovered, is particularly radio-loud, and particularly bright in hard X-rays (Courvoisier, 1998). The broad-band spectrum of 3C 273 is dominated by the unresolved nucleus, including the accretion disk, disk corona, and small-scale jet. The source can be considered as a slightly misaligned FSRQ, observed at intermediate angles of about  $\sim 10^\circ$ . The extensive X-ray monitoring of 3C 273 over about 30 years using different instruments established a variability of the source on the timescales from years (flux changes by a factor of a few/several) down to days (a few/few tens percents; Johnson et al., 1995; Kataoka et al., 2002; Courvoisier et al., 2003; Chernyakova et al., 2007; Soldi et al., 2008). The compilation of broad-band multi-epoch spectra reveals in addition that in the hard X-ray regime (above 10 keV, roughly) the characteristic variability timescales are longer and the variability amplitudes are larger than those in the soft/medium X-ray regime. The X-ray variability properties suggest therefore a presence of two separate components: one most likely a Seyfert-like, related to the accreting matter, and the other a blazar-

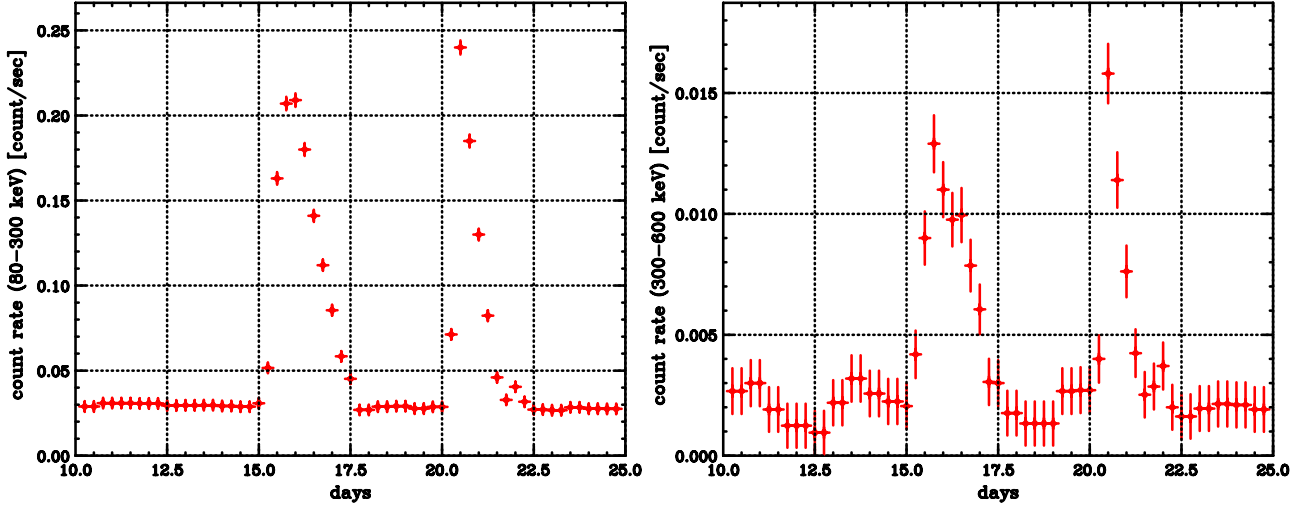


**Figure 7:** Simulated SGD lightcurve 3C 273 in two energy channels 80–300 keV (left panel) and 300–600 keV (right panel), with 6 h binning, assuming a linear correlation of the X-ray flux and the GeV flux as detected with *Fermi*-LAT during the 2009 outburst (Abdo et al., 2010c).

like jet, produced via inverse-Comptonization of soft photons by low-energy electrons. This idea is in accord with the fact that the X-ray spectrum of 3C 273 in the soft band is steep ( $\Gamma > 2$ ), while it is relatively flat in the medium and hard bands ( $\Gamma \simeq 1.7 \pm 0.2$ , up to the MeV range). A marginal detection of weak fluorescent Fe lines in 3C 273 has been reported only in some epochs.

We have simulated the hard X-ray spectrum of 3C 273 observed with *ASTRO-H* for different exposure times, assuming the average flux and photon index from the 58 month *Swift*-BAT catalog, namely  $\Gamma = 1.73$  and  $F_{14-195\text{ keV}} = 4.3 \times 10^{-10} \text{ erg cm}^{-2} \text{ s}^{-1}$ . The spectrum is characterized well in a broad energy range with exposures as short as 30 ks, for which the joint HXI and SGD fit returned  $\Gamma = 1.732 - 1.743$ ,  $F_{5-80\text{ keV}} = (3.43 - 3.47) \times 10^{-10} \text{ erg cm}^{-2} \text{ s}^{-1}$ , and  $F_{40-600\text{ keV}} = (5.69 - 5.85) \times 10^{-10} \text{ erg cm}^{-2} \text{ s}^{-1}$ . In shorter exposures 3C 273 is still clearly detected, although its spectral properties above 200 keV cannot be accessed robustly. The Fe line is also easily detectable at the average flux level with the SXS assuming that this is narrow (from the illuminated torus) rather than from the illuminated inner disc.

3C 273 was established as a high-energy  $\gamma$ -ray source by the EGRET instrument onboard the CGRO (Hartman et al., 1999). More recently, continuous monitoring of the source with *Fermi*-LAT resulted in the detection of prominent flares at GeV photon energies (Abdo et al., 2010c). This  $\gamma$ -ray emission is widely believed to originate in the jet, and to constitute the high-energy tail of the inverse-Compton component which first pops-up in hard X-rays. Hence, *simultaneous* *ASTRO-H* and *Fermi*-LAT observations of 3C 273 may uniquely constrain the spectral evolution of the radiating jet electrons over a particularly broad range of energies, and on short timescales which have been never probed before at hard X-rays in this source or, in fact, in any blazar. We note in this context that 3C 273 is much more prominent in X-rays than even the brightest FSRQs (in their quiescence), since even though the jet emission in FSRQs is more significantly beamed due to their small jet inclinations, they are more distant objects.

In order to illustrate this point, we have simulated the SGD light curve of 3C 273 in two energy channels, assuming a linear correlation of the X-ray flux with the GeV flux as detected with *Fermi*-LAT during the large outburst in 2009 (Abdo et al., 2010c). The results are presented in Figure 7. As shown, the SGD observations will indeed allow for a unique characterization of the hard X-ray variability in the source down to the timescales of 6 h, with one-to-one comparison between the lightcurves in different X-ray and  $\gamma$ -ray bands. The jet variability robustly constrained in this way at high-energies may be next juxtaposed with the variability of the accretion-related soft X-ray continuum probed with the SXS.

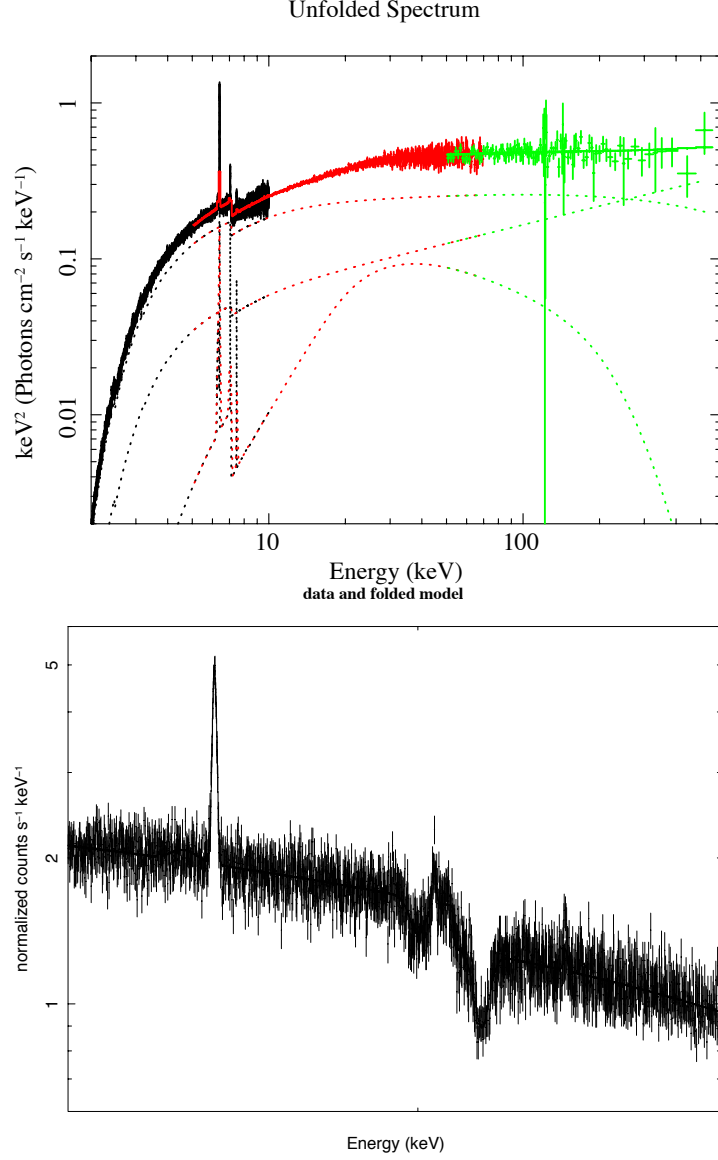


**Figure 8:** Upper: Simulated broad-band spectrum of Centaurus A with 100 ks exposure, based on the spectral parameters taken from Fukazawa et al. (2011b), with SXI shown in black, HXI in red, and SGD in green. The fitted model shown with dotted curves includes the absorbed power-law representing the disk/corona component, the additional power-law related to the jet, and the torus reflection component. Lower: 6–8 keV SXS simulation of blue-shifted absorption lines in the Centaurus A spectrum for 100 ks exposure. Here we assumed two absorption lines at 7.0 keV and 7.2 keV with the line width of 25 eV and the normalizations of  $-5.6 \times 10^{-5} \text{ ph cm}^{-2} \text{ s}^{-1}$ .

### 3.2 Radio Galaxy Centaurus A

The low-power radio galaxy Centaurus A is the nearest AGN (distance of 3.7 Mpc), known for its complex radio structure and post-merger host galaxy (see Israel, 1998). It is one of the brightest hard X-ray/soft  $\gamma$ -ray emitter in the sky, detected by all the instruments onboard the CGRO during the period 1991-1995 (see Steinle et al., 1998, and references therein). More recently, the central regions of Centaurus A have been also resolved with *Fermi*-LAT (Abdo et al., 2010d) and H.E.S.S. (Aharonian et al., 2009) at high and very-high energy  $\gamma$ -rays, respectively. The origin of the observed  $\gamma$ -rays is puzzling: on the one hand, the steep  $\gamma$ -ray continuum seems to resemble a misaligned blazar component, while on the other hand this continuum joins smoothly with the X-ray continuum, which is in fact most likely related to the accreting matter in the source; in addition, the TeV emission seems in excess of the extrapolated GeV continuum, suggesting either a separate spectral component,



or a non-standard emission spectrum (see the discussion in Abdo et al., 2010d). The broad-band characteristics of the X-ray emission of Centaurus A are therefore of a particular importance for understanding this archetypal AGN, and several observational studies have been dedicated in the past to this problem (Evans et al., 2004; Markowitz et al., 2007; Fukazawa et al., 2011b; Beckmann et al., 2011). For example, based on the variability analysis from multiple deep *Suzaku* pointings, Fukazawa et al. (2011b) argued for a dominant jet contribution only above 100 keV; however, the limit of  $\sim 250$  keV on the energy range of the *Suzaku* XIS and HXD precluded any definitive conclusions.

The broad-band coverage and high sensitivity of the *ASTRO-H* HXI and SGD instruments will allow us to search for a spectral cutoff in the hard X-ray/soft  $\gamma$ -ray spectrum of Centaurus A, expected in the case of a dominant disk corona component, to look for polarization signatures around 100 keV photon energies, which may be expected in the case of a pronounced jet component, and in general to constrain precisely the slope of the X-ray continuum in the hard X-ray/soft  $\gamma$ -ray range. Figure 8 (left) presents the simulated broad-band *ASTRO-H* spectrum of the source in 100 ks exposure (based on the parameters from Fukazawa et al., 2011b).

However, detailed soft X-ray spectroscopy of the target with the SXS are expected to be equally revealing. First, the Fe-K line in Centaurus A is the second brightest after that in the Circinus galaxy, with the equivalent of about 80 eV. The SXS can measure precisely the line width and Compton shoulder, which in turn, when assessed jointly with constraints from the broad-band continuum study of the reflection bump around 50 keV, will constrain the location and geometry of the neutral reflector in the source.

Second, we note that the presence of the two absorption lines from Fe XXV He  $\alpha$  at  $E = 6.7$  keV (EW  $\approx 10$  eV) and Fe XXVI Ly  $\alpha$  at  $E = 6.96$  keV (EW = 15 eV) was reported in the three *Suzaku* observations of Centaurus A performed in 2009 (Tombesi et al., 2014). The lines are detected with a high significance of  $> 99.99\%$ . However, due to the limited energy resolution of the *Suzaku* XIS, these lines were not resolved and also the outflow velocity of the absorber could not be constrained. Hence the line origin (outflowing wind versus the extended ionized absorber with no net velocity) remains an open question. Accordingly to our simulations based on the line modeling with an XSTAR table, the unprecedented energy resolution of the SXS will allow us to resolve these lines with high accuracy in the exposures as short as 100 ks (see Figure 8, right panel), and to measure the velocity of the absorber, thus providing robust constraints on the line origin.

### 3.3 UFOs and Radio-Loud AGN

A systematic analysis of the *Suzaku* spectra of a small sample of five bright BLRGs performed by Tombesi et al. (2010a) revealed blue-shifted Fe XXV/XXVI K-shell absorption lines at  $> 7$  keV energies at least in three of them, namely 3C 111, 3C 120 and 3C 390.3. These lines originate from highly ionized and high column density gas outflowing with very high velocities, from  $\sim 1,000$  km s $^{-1}$  up to mildly-relativistic values of the order of 40% of the speed of light, which are referred to as ultra-fast outflows (UFOs). Successive studies found similar outflows also in 3C 445 and 4C+74.26 (Reeves et al., 2010; Gofford et al., 2013). Later, the search for such absorption lines was extended to a large sample of 26 radio-loud AGN observed with *XMM-Newton* and *Suzaku* (Tombesi et al., 2014). Combining the results of this analysis with those in the literature and correcting for the number of spectra with insufficient signal-to-noise, the incidence of UFOs in radio-loud AGN was estimated to be in the range 30-70%. This indicates the presence of complex accretion disk winds in a significant fraction of sources.

Ultra-fast outflows found in radio-loud AGN are similar to the UFOs reported in  $> 40\%$  of radio-quiet AGN (e.g., Tombesi et al., 2010b; Gofford et al., 2013, see the “AGN Winds” *ASTRO-H* White Paper), suggesting that any jet-related radio-quiet/radio-loud dichotomy might not apply to AGN winds. The typical location of the UFOs is estimated to be in the range  $\sim 10^2 - 10^4 r_s$  from the central SMBH, where  $r_s = GM_{BH}/c^2$  is the black hole gravitational radius. The study of UFOs in radio-loud AGN can therefore provide important insights into the characteristics of the innermost jet launching regions, where the collimation and the bulk acceleration of initially broad and only mildly-relativistic electromagnetic jets is expected to take place (e.g., McKinney, 2006; Tchekhovskoy et al., 2011; Sądowski et al., 2014).

One of the most relevant and promising targets for exploring the presence and the energetics of the disk



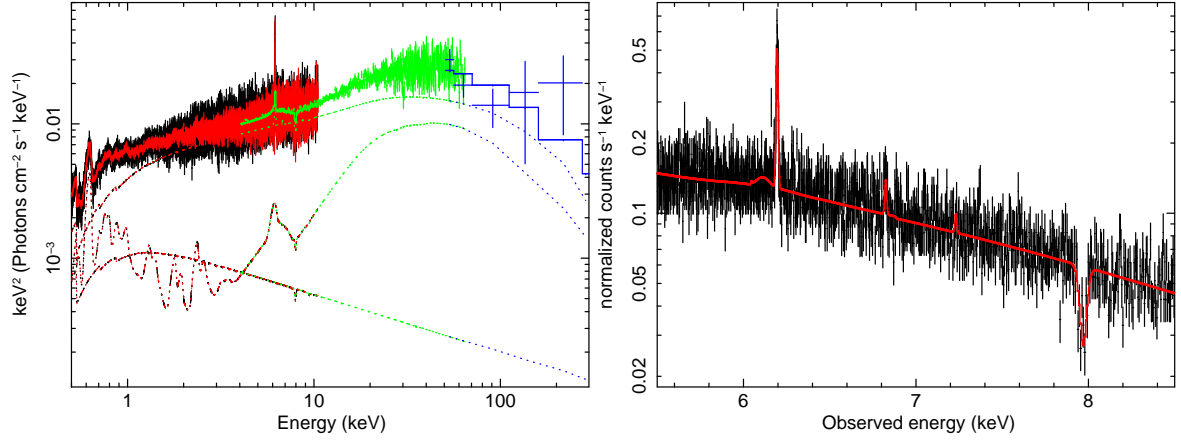


**Figure 9:** Left: Simulated 100 ks *ASTRO-H* broad-band spectrum of 3C 120 in the range 0.5 – 300 keV, corresponding to the state in which the jet knot is ejected and the inner disk is disrupted (the inner disk radius recedes from  $r_{in} \simeq r_g$  up to  $r_{in} \simeq 38 r_g$ ). The SXS spectrum is shown in black, the SXI in red, the HXI in green, and the SGD in blue. Right: Zoomed SXS spectrum in the Fe K band (5–8.5 keV).

winds in the particular context of the jet/disk coupling in AGN is the nearby radio galaxy 3C 120 ( $z = 0.033$ ). Previous X-ray monitoring of the source, augmented by high-resolution radio data, hint at a close link between the disk state transitions and the jet formation processes, manifesting as major X-ray dips in the accretion disk corona lightcurve followed by ejections of bright superluminal knots in the radio jet (see Marscher et al., 2002; Chatterjee et al., 2009). More recently, Lohfink et al. (2013) presented the in-depth study of the central engine in the source using a multi-epoch analysis of the deep *XMM-Newton* observation and the two deep *Suzaku* pointings. The authors discussed a composite source model consisting of a truncated/refilling disk during the *Suzaku* observations, and a complete disk extending down to the innermost stable circular orbit (ISCO) during the *XMM-Newton* observation. The ejection of a new jet knot was observed approximately one month after the analyzed *Suzaku* pointings, and Lohfink et al. (2013) argued that this might indicate the timescale for propagation of a disturbance from the disk into the jet.

The 2 – 10 keV flux of 3C 120 varied over the range  $2 - 6 \times 10^{-11} \text{ erg cm}^{-2} \text{ s}^{-1}$  in the long-term *RXTE* monitoring analyzed in Chatterjee et al. (2009). In our simulations below we therefore assume conservatively the lowest flux of the target. We consider the combined disk-jet model of Lohfink et al. (2013), in which the jet X-ray emission is parameterized by a steep power-law with the photon index of 2.5 – 4, while the disk corona continuum is represented by a power-law component with the photon index of 1.7 – 2.4 with a high energy cut-off at 150 keV. In the first considered case, the disk extends down to the ISCO. This is modeled in XSPEC with a relativistically blurred (kdblur) ionized reflection component (reflionx) for the inner disk radius  $r_{in} \simeq r_g \simeq 0.86 \times 10^{13} \text{ cm}$ ,  $q \simeq 7$ , inclination  $i \simeq 15^\circ$ , and the ionization  $\xi \simeq 200 \text{ erg cm s}^{-1}$ ; the neutral distant reflector (pexmon) is included with the reflection fraction  $R \simeq 2$ . In the second case, which is related to the launch of the jet knot, the inner disk is disrupted and the inner radius recedes to  $r_{in} \simeq 38 r_g$ ; the relativistic blurred reflection has now a more standard  $q$  value of  $\simeq 3.5$  and the neutral reflection factor is  $R \simeq 0.26$ . The ultra-fast outflow with the velocity  $v_{out} \simeq 0.161 c$  was detected by (Tombesi et al., 2014) in this latter state. The outflow is modeled below with the XSTAR table assuming a turbulent velocity of  $3,000 \text{ km s}^{-1}$ , ionization  $\log \xi \simeq 4.9 \text{ erg cm s}^{-1}$ , and column density  $N_H \simeq 5 \times 10^{22} \text{ cm}^{-2}$ . When modeled with an inverted Gaussian absorption line, this is equivalent to energy  $E \simeq 8.23 \text{ keV}$ , intrinsic line width of  $\sigma \simeq 110 \text{ eV}$ , and  $\text{EW} \simeq -20 \text{ eV}$ .

The simulated *ASTRO-H* broad-band spectrum of 3C 120 in 100 ks exposure, corresponding to the latter state described above, is shown in Figure 9. The source is detected at high significance with all the instruments onboard, from 0.5 keV up to 300 keV. This will simultaneously constrain the corona power-law continuum, the jet emission component, and the neutral/ionized reflection. In particular, the accuracy in the determination of the power-law slopes, cut-off energy, reflection fraction, and the ionization parameter, will be of 2%, 25%, 10% and 10%, respectively. In addition, the inner disk radius will be measured with the 15% accuracy. Moreover,

the presence of the disk wind will be determined by means of the Fe K UFO at the  $>5\sigma$  level. The energy, width, and the equivalent width of the line will be determined at the 0.5%, 20% and 20% levels, respectively. Finally, the velocity and ionization of the UFO will be constrained at the 2% and 10% levels, respectively. These will allow for a direct and truly simultaneous comparison between the activity level of the intermittent jet, the state of the accretion disk, and the energetics of the disk wind. We note that 3C 120 is systematically monitored on a daily basis in  $\gamma$ -rays with *Fermi*-LAT (see in this context Kataoka et al., 2011), approximately once per week at optical frequencies with KANATA, and roughly in the monthly cadence at radio frequencies with high and low-resolution interferometers through several projects, such as the MOJAVE or the F-Gamma projects.

## 4 Starburst-AGN Connection in Nearby Galaxies

Several nearby galaxies host both a prominent AGN and a nuclear starburst. Disentangling the two emission components in such sources is essential for constraining their overall energetics, and for understanding galaxy evolution processes in general. However, this task requires simultaneous, truly broad-band, and high-quality X-ray spectra, which are rarely available even for the brightest systems. As argued below, this may change significantly in the near future with *ASTRO-H*.

Some of the starburst/AGN systems are now also established  $\gamma$ -ray emitters, including the two cases discussed below, namely NGC 4945 and Circinus galaxy (Ackermann et al., 2012; Hayashida et al., 2013, respectively). The observed  $\gamma$ -ray emission of such sources is believed to originate predominantly in the starburst regions via cosmic rays produced by supernova explosions interacting with the interstellar medium. Yet in some cases the origin of the  $\gamma$ -ray photons detected with *Fermi*-LAT is an open issue, as for example the Circinus galaxy appears over-luminous at GeV energies with respect to the expected starburst emission given its far-infrared and radio luminosities (see Hayashida et al., 2013). The difficulty is, however, that the starformation rate in this system, estimated from the radio-to-IR data, is rather uncertain, translating to large uncertainties in the expected cosmic ray luminosity. *ASTRO-H* observations may help to resolve this problem, which is very relevant as  $\gamma$ -ray observations are now widely considered as an important, newly emerging window into the action of starformation processes in the evolving galaxies.

### 4.1 Circinus Galaxy

The Circinus galaxy, at a distance of  $\sim 4$  Mpc, hosts a Compton-thick AGN and shows evidence of starburst activity. It is thus an excellent laboratory for studying the X-ray reprocessor in a heavily obscured system, as well as studying the interplay between AGN activity and star-formation. The broad-wavelength *ASTRO-H* coverage, from the SXI to HXI and SGD, together with the high resolution capabilities of the SXS will provide unprecedented insight into the obscuring medium, and constrain the relative contribution of photo-ionization and collisional ionization to the soft X-ray emission.

With the advent of models, such as MYTorus (Murphy & Yaqoob, 2009) that self-consistently treat the effects of the transmitted, Compton scattered and fluorescent line emission in obscured AGN, we are able to analyze the X-ray spectrum of Compton-thick AGN in a physically meaningful way. Currently, the most comprehensive X-ray analysis of Circinus involves simultaneous *NuSTAR* and *XMM-Newton* observations (Arevalo et al., 2014), which included archival *Chandra* data to model the nuclear only region ( $3''$ ) and contamination within the *NuSTAR* FOV from an X-ray binary (CGX1) and supernova remnant (CGX2, see Figure 10). The X-ray binary is highly variable in X-rays: for the best constraints on modeling the AGN emission and details of the X-ray reprocessor, a simultaneous *Chandra* ACIS-S observation is required. In combination with coverage from 0.5–500 keV with *ASTRO-H* this will provide the best measurements on physically meaningful modeling. This will enable us to derive constraints on the line-of-sight and global column density, from which we can calculate the intrinsic X-ray luminosity, extending the bandpass visible by *NuSTAR* to lower energies ( $<3$  keV) and higher energies ( $>80$  keV).

To estimate the low-resolution *ASTRO-H* spectra of Circinus, we set up models using published fits to archival data, where the low-resolution SXI spectrum is based on the *XMM-Newton* fit reported in Massaro et al. (2006) and the HXI spectrum uses the joint *NuSTAR*, *Suzaku* PIN, *BeppoSAX* and *Swift*-BAT fit from Arevalo et al. (2014) as a template. As shown in Figure 11, a 100 ks *ASTRO-H* observation would provide extremely high signal-to-noise in the low-resolution spectra. The high-resolution SXS spectrum will enable the Compton-shoulder around the Fe  $K\alpha$  6.4 keV line to be modeled, imparting information about the opening angle that may not be apparent with lower resolution spectra (see the “AGN Reflection” *ASTRO-H* White Paper). Neither CGX1 or CGX2 have strong neutral Fe  $K\alpha$  emission (Bauer et al., 2001) and would therefore not contaminate the nuclear Fe  $K\alpha$  and Compton-shoulder emission.

As depicted in Figure 10, *Chandra* observations of Circinus reveal that diffuse emission is associated with the active nucleus as well as an ionization cone extending north-west above the AGN which contributes  $\sim 15\%$  to the extended emission (Sambruna et al., 2001a). Modeling the circumnuclear and extended diffuse emission in the low-resolution *Chandra* ACIS spectra reveals both thermal and non-thermal contributions, where the observed Fe  $K\alpha$  emission likely results from Compton-scattering of the AGN continuum (Arevalo et al., 2014). The simultaneous 0.5–500 keV *ASTRO-H* coverage will enable the starburst contribution to be disentangled from the AGN component: the 2–500 keV spectrum will allow the tightest constraints on modeling the AGN continuum, isolating the starburst component at lower energies.

Further details of the relative amount of starburst to AGN activity can be provided by high-resolution spectroscopy from SXS. *Chandra* grating analysis reveals that the circumnuclear emission results from both photoionization and photoexcitation, i.e., reprocessed AGN emission rather than star-formation (Sambruna et al., 2001b). As shown in Figure 12, a 100 ks *ASTRO-H* observation, based on the *Chandra* and *XMM-Newton* modeling of the circumnuclear region (Massaro et al., 2006), will provide a spectrum with high signal-to-noise in the emission lines. Using diagnostics such as the radiative recombination continua (RRC) and the ratios of forbidden ( $f$ ), inter combination ( $i$ ), and resonance ( $r$ ), lines in the OVII triplet, gives the relative amount of photoionization and collisional ionization. For instance, a narrow RRC feature indicates that the plasma is photoionized (Liedahl & Paerels, 1996) while the ratio  $G = (f + i)/r$  exceeds 4 in photo ionized plasma and is  $\sim 1$

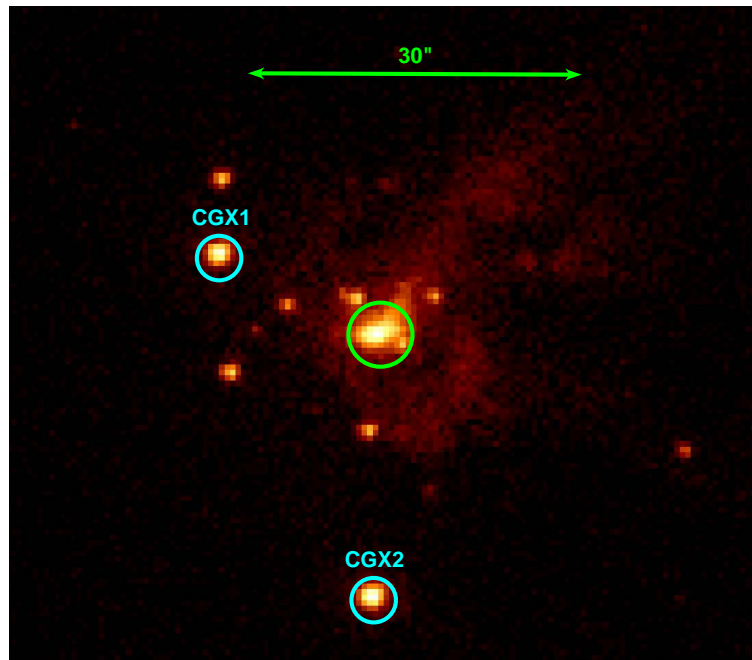


**Figure 10:** *Chandra* ACIS image of Circinus, where the green circle indicates the nucleus and the cyan circles show strong X-ray point sources that will contribute to the emission observed by *ASTRO-H*. Diffuse emission from the circumnuclear starburst ring and the north-west ionization cone is also visible.

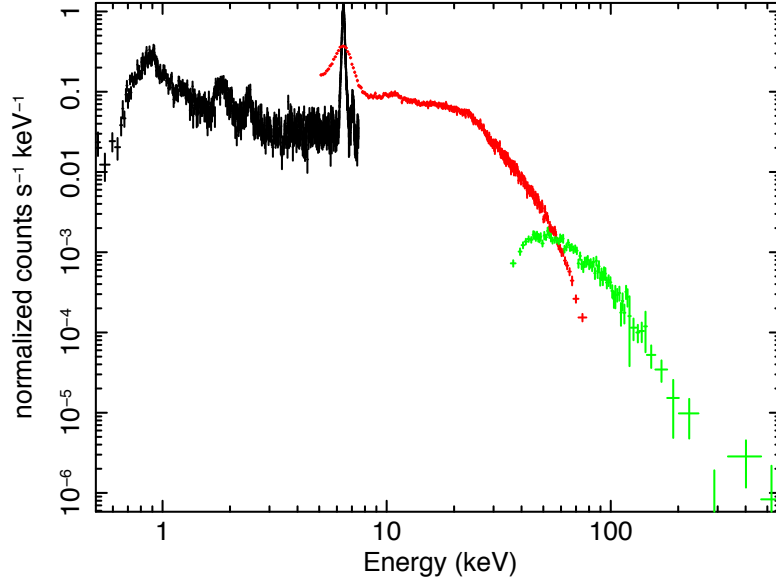


**Figure 11:** Simulated low-resolution 100 ks *ASTRO-H* spectrum of Circinus (SXI shown in black, HXI in red, and SGD in green) based on the modeling by Massaro et al. (2006), Arevalo et al. (2014), and Yang et al. (2009).

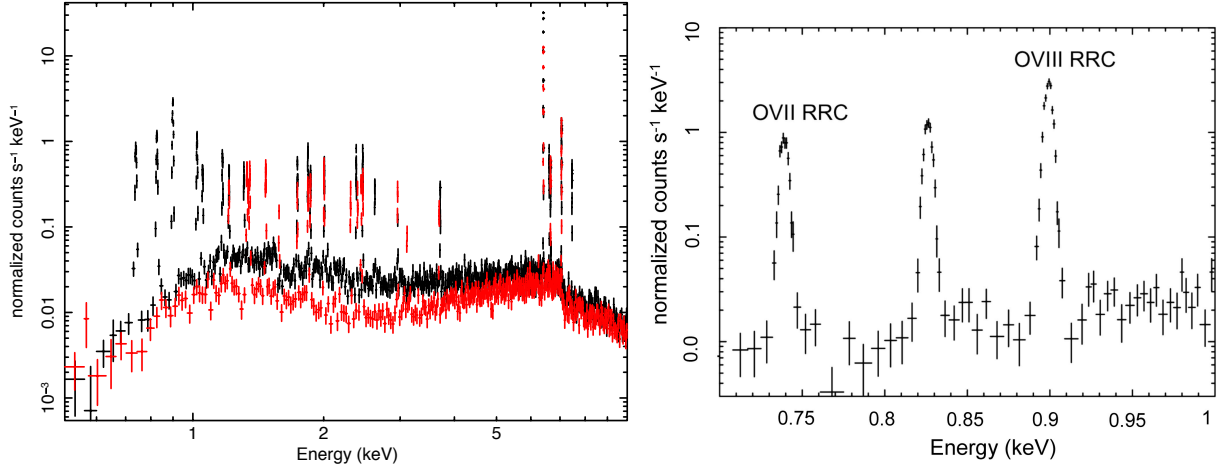


**Figure 12:** Left: Simulated 10 ks SXS spectra of Circinus, where the black spectrum is based on the *XMM-Newton* RGS fit and the red spectrum is based in the *Chandra* HETG fit presented in Massaro et al. (2006). Right: Close-up of the OVII RRC and OVIII RRC features which will be prominent in a 100 ks observation. The widths of these lines will diagnose the relative starburst to AGN contribution to the observed X-ray emission.

when collisionally ionized (Porquet & Dubau, 2000). Based on the *XMM-Newton* RGS spectra of Circinus, the OVII RRC (0.739 keV) and OVIII RRC (0.899 keV) features will be prominent in a 100 ks SXS observation, as shown in Figure 12 (right). The plasma diagnostics that can be studied with SXS will represent an improvement upon previous HEG and RGS analysis.

## 4.2 NGC 4945

NGC 4945 is the brightest radio-quiet Seyfert 2 in hard X-rays (Done et al., 1996), as well as the closest bona fide Compton-thick AGN (Iwasawa et al., 1993). It lies in a nearby (distance of 3.7 Mpc) edge-on spiral galaxy with a highly obscured nucleus containing a composite starburst/AGN system (Moorwood & Oliva, 1994). The nucleus also appears to be obscured at mid-infrared wavelengths (Krabbe et al., 2001; Asmus et al., 2014; Gandhi et al., 2014), with the starburst being energetically dominant over the full optical and infrared regime (Moorwood et al., 1996; Goulding & Alexander, 2009). A starburst ring  $\sim 200$  pc in diameter has been imaged

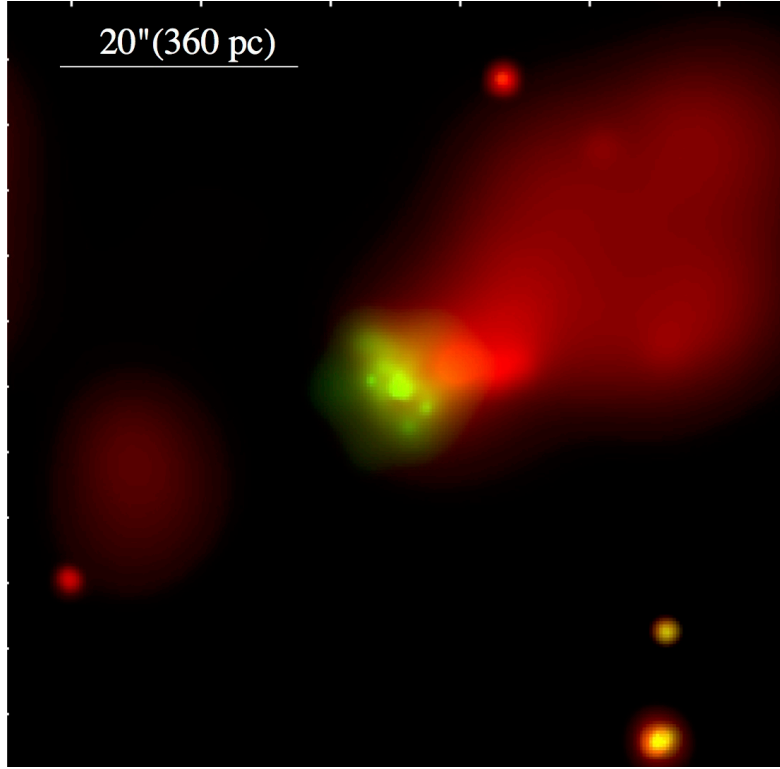


**Figure 13:** Direct imaging of the core of NGC 4945 with *Chandra* (red: 0.3–2 keV is dominated by extended emission, presumably associated with the starburst; green: 2–10 keV emission is associated with the reflector). Note that the reflector is resolved. The field of view is 1 arcmin on a side (Credit: Marinucci et al. 2012).

in the system (Marconi et al., 2000). At subarcsecond scales, a compact radio source is detected, along with a 5 pc–long jet (Elmouttie et al., 1997; Lenc & Tingay, 2009). A megamaser is known to exist in the nucleus, and VLBI mapping has determined a black hole mass of  $1.4 \times 10^6 M_{\odot}$  (Greenhill et al., 1997). NGC 4945 was also detected with *Fermi*-LAT (Ackermann et al., 2012). Although the origin of the observed  $\gamma$ -ray emission is not fully resolved, the detected GeV flux is consistent with expectations from starburst emission.

Despite its proximity, NGC 4945 remains one of the least understood of Compton-thick AGN. It is the best example of only a handful of Compton-thick AGN known to vary strongly above 10 keV. This variation implies that scattering from circumnuclear clouds does not completely suppress the direct component at hard X-ray energies which, in turn, argues in favor of a small covering factor of the circumnuclear ‘torus’ (Madejski et al., 2000). This has been confirmed from broadband spectral analyses in a number of studies (e.g. Itoh et al., 2008; Yaqoob, 2012; Puccetti et al., 2014). Direct imaging with *Chandra* has resolved the reflector around the nucleus and found it to be located at large nuclear distances ( $\sim 30$  pc) rather than being associated with a classical sub-pc scale torus (Marinucci et al., 2012). This is shown in Figure 13. Clumpy reflecting clouds appear to be mixed in with the extended starburst ring. A *Chandra*/HEG observation has found a broad component to the Fe  $K\alpha$  line at a full-width-half-maximum (FWHM) of  $2780^{+1110}_{-740}$  km s $^{-1}$  ( $1-\sigma$  uncertainty; Shu et al. 2011). As discussed by Yaqoob (2012), this broadening may be related to the spatial extent of the line, and the presence of a classical sub-pc scale torus has not been definitely established in NGC 4945; if it exists, it appears to be geometrically-thin, a unique property amongst the nearby Compton-thick AGN.

The source shows accretion episodes with luminosities of up to at least 30% of the Eddington luminosity (Puccetti et al., 2014). This is a factor of about 10 larger than the mean Eddington rates inferred for the local *Swift*-BAT AGN population (Vasudevan et al., 2010). It is unknown whether the Compton-thick obscurer on large scales is providing the fuel necessary for this growth, or whether strong radiative feedback is responsible for driving away matter and rendering the torus geometrically-thin and clumpy. The high energy cut-off ( $E_{\text{cut}}$ ) to

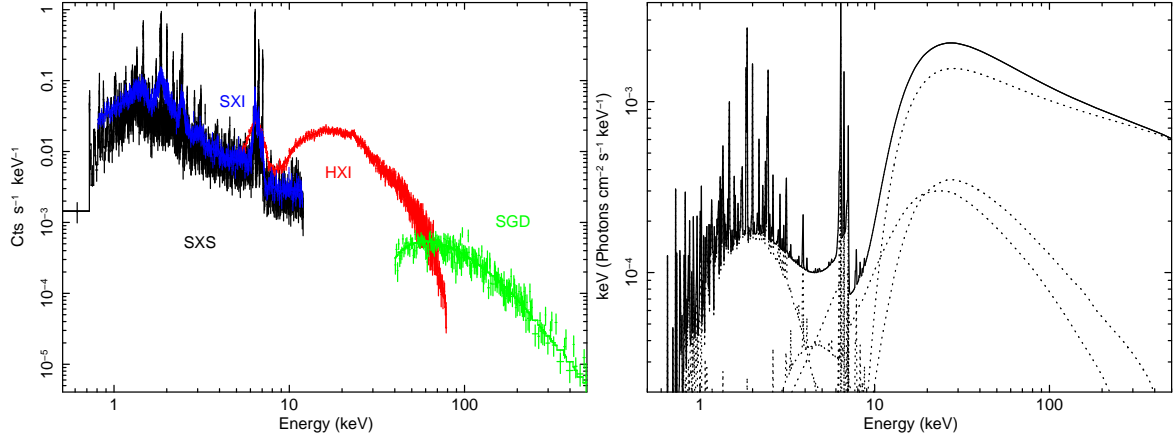


**Figure 14:** *ASTRO-H* simulation of NGC 4945 with 150 ks of exposure, assuming the median flux model M from the *NuSTAR* observation reported in Puccetti et al. (2014). The counts spectra for SXS, SXI, HXI and SGD are shown on the left, and the model is shown on the right, in  $F_E$  units. The model includes three thermal components at soft energies, a power-law intrinsic continuum and two decoupled MYTorus components (edge-on and pole-on) for the Compton-thick absorber/reflector. A simple absorbed power-law ( $\Gamma = 2.2$ ; not shown) can describe the contribution of contaminating sources within the host galaxy at the level of 50% of the 4–6 keV flux. These contaminants display no Fe line emission.

the direct power-law which can constrain the shape of the intrinsic continuum has not yet been securely detected in NGC 4945. Using *NuSTAR*, Puccetti et al. (2014) determined a loose constraint on  $E_{\text{cut}} = 190^{+200}_{-40}$  keV in a high flux state, but could only place lower limits of 200–300 keV on  $E_{\text{cut}}$  in median and low flux states. It remains to be determined whether  $E_{\text{cut}}$  is dependent upon source flux. Note that these lower limits lie beyond the energies that can be easily constrained with *Swift*-BAT.

The unknown coronal properties at hard X-rays and poorly understood reflector properties at soft energies make NGC 4945 an ideal target for broadband observations with *ASTRO-H*. The high resolution spectroscopic capability of SXS will allow resolved measurements of the iron line fluxes and widths, and can provide the first constraints on the profile shapes. From the broadest component of the Fe  $K\alpha$  line, the SXS will locate the distance ( $r$ ) of the innermost reflector, which can be compared with torus models. This will give a direct answer to the question of whether a classical sub-pc Compton-thick torus exists in NGC 4945 or not. Grating spectrometer observations from the *Chandra*/HEG cannot distinguish spatial broadening of lines from spectral broadening. The 5 eV spectral resolution of SXS will allow searches for sub-structure to within  $1/10^{\text{th}}$  the line width of about  $2800 \text{ km s}^{-1}$  inferred from HEG observations by Shu et al. (2011), and so will quantify the strength of any single broad profile due to the inner torus vs. broadening due to the extended reflector.

In addition, the SXS will shed light on the power source of the ionized lines as due to either a collisionally-ionized or photo-ionized plasma, by measurement of ionized line ratios. If the reflector itself is strongly photo-ionized, this may partly explain the low reflection fraction. With regard to the low covering factor of the reflector, this could be related either to torus clumpiness or to a geometrically-thin configuration, or a combination of the two. The iron line profiles will constrain the geometrical distribution of the reflector. The Fe  $K\alpha$  and  $\beta$  lines will determine the ionization state. Combined with the reflector location, the ionization parameter ( $\xi = L/nr^2$ ), and hence density ( $n$ ) can be determined. Clumpiness can then be constrained by combining the observed line luminosity,  $n$  and column density ( $N_{\text{H}} = nr$ ).

Measurement of the iron line central energies and line profiles will constrain torus kinematics. If there is significant radiative feedback as a result of the high Eddington fraction, this may affect the matter distribution on large scales, e.g. resulting in an outflow. Recently, interferometric observations have revealed dusty outflows in mid-infrared emission (Hönig et al., 2013). Dust velocities cannot be measured in the mid-infrared though these are expected to be similar to warm absorber velocities of several hundred  $\text{km s}^{-1}$ . If the dust is entrained with the X-ray-fluorescing gas, iron line kinematics will directly measure the outflow velocities. Although some constraints on the line kinematics are available from the *Chandra*/HEG analysis by Shu et al. (2011), these



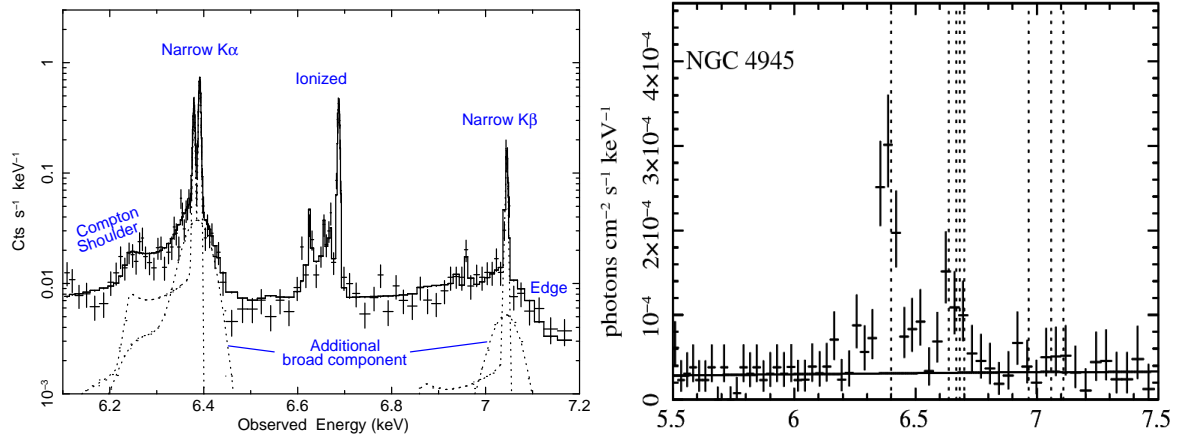


**Figure 15:** Left: Zoom-in on the iron line complex including neutral  $K\alpha$ ,  $K\beta$  and the ionized lines for the 150 ks broadband simulation shown in Figure 14. The narrow line components are assumed to have intrinsic widths (full-widths-at-half-maximum; [FWHM]) of  $100 \text{ km s}^{-1}$ , as may be expected on extended ( $\sim 30 \text{ pc}$ ) scales where the bulk of the reflector is seen to be located with *Chandra* (Marinucci et al., 2012). In addition, a potential underlying broad component simulating fluorescence from the walls of the inner torus (whose existence is uncertain thus far), has been included as a MYTorusL (fluorescence) component smoothed with a Gaussian of  $\text{FWHM} = 2800 \text{ km s}^{-1}$  and normalized to contain half of the total  $K\alpha$  line flux. This inner torus emission can clearly be distinguished from the narrower extended components in  $K\alpha$ . The most prominent  $K\alpha$  and  $\beta$  model components are shown as the dotted lines. Right: The best spectral resolution data on the iron complex available until now (*Chandra* High Energy Grating observation of NGC 4945, as reported by Shu et al. 2011).

are based on single Gaussian fits to the entire  $K\alpha$  complex and include the narrow doublet, Compton shoulder and any underlying broad component. The SXS will enable deconvolution of these various components and allow much better constraints on the kinematics. Finally, and importantly, *ASTRO-H* will provide a sensitive measurement of the intrinsic continuum shape, especially the high energy cutoff.

We simulated a 150 ks exposure with *ASTRO-H*, assuming the model parameters of the median flux state *NuSTAR* observation reported by Puccetti et al. (2014). The latest instrument responses available on the *astroh-cal* wiki page as of May 2014 were employed. This model includes three thermal components to account for emission from the superwind known in this system (Schurch et al., 2002), and a direct power-law of photon-index  $\Gamma = 1.88$  obscured by a column density  $N_{\text{H}} = 3.6 \times 10^{24} \text{ cm}^{-2}$ . The torus reflector is modeled with the MYTorus code (Murphy & Yaqoob, 2009) with decoupled transmission and scattering normalizations to account for the source complex emission properties (e.g. clumpiness, non-solar abundances etc.), resulting in an effective covering fraction of 0.16. Additional emission from Fe XXV is also included, as reported by Puccetti et al. (2014). The result is shown in Figure 14, and a zoom-in on the Fe complex is shown in Figure 15.

The SXS will clearly measure the Fe line central energies and widths. Towards the red side of the Fe  $K\alpha$  line, the Compton shoulder will be easily detectable and will shed light on the origin of the iron fluorescence emission as either reflection or transmission. Previous high spectral resolution observations with *Chandra*'s High Energy Grating are also shown in the figure. The simulated SXS spectrum has far superior sensitivity to the *Chandra* data in terms of both line detection as well as characterization.

The origin of the broad component is unclear from the *Chandra* data, and one promising origin may be in an inner torus reflector characterized by line velocities similar to the Broad Line Region. In order to test whether such a component can be separated from the narrow components, we added in a broad component with  $\text{FWHM} = 2800 \text{ km s}^{-1}$  to the baseline model inferred from *NuSTAR*. This was simulated using a smoothed MYTorusL fluorescence spectrum. The normalization of this inner torus broad component is taken to be half of the total Fe  $K\alpha$  line flux (Marinucci et al. 2012 estimated that about half of the Fe line seen with *Chandra* may be spatially unresolved). As shown in Figure 15, the inner (broad) and outer (narrow) torus reflection components can be clearly distinguished. The fractional error on the FWHM of this broad component when fitting the simulated spectrum is  $\approx 0.13$ , i.e. 13% of the assumed intrinsic FWHM, which is  $350 \text{ km s}^{-1}$  (90% confidence). The observation will be sensitive enough to detect the presence of sub-structure in addition to any

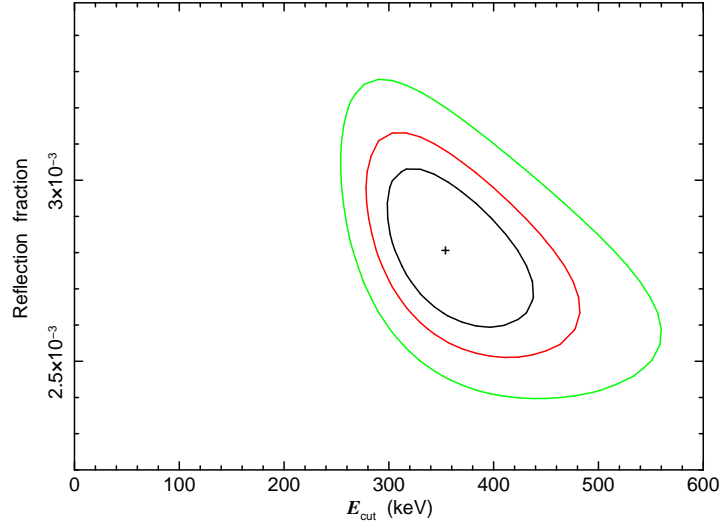


**Figure 16:** Confidence contours for a fit to the reflection fraction and  $E_{\text{cut}}$  for the simulated 150 ks exposure of NGC 4945, assuming  $E_{\text{cut}} = 400$  keV. The contours are for  $\Delta\chi^2$  changes corresponding to 68%, 90% and 99% confidence, for two parameters of interest.  $E_{\text{cut}}$  can be constrained well beyond energies constrained thus far.

single broad component.

The ionized line around 6.7 keV is also apparent in the spectrum, with the resonance, forbidden and inter-combination lines all potentially resolvable if the velocity spread is low. Flux ratios between these lines can distinguish between collisionally ionized and photo-ionized plasma, and thus shed light on the connection between the AGN and starburst emission. Finally, the Fe edge and Ni  $K\alpha$  (latter not shown) are also detectable and will place important constraints on elemental abundances.

The combination of HXI and SGD will constrain  $E_{\text{cut}}$  to higher energies than possible before. The MYTorus model above does not include a high energy cutoff. So, in order to simulate the cutoff, we approximated the continuum above 10 keV as a combination of the absorbed power-law from Puccetti et al. (2014) and a pure reflection PEXRAV component. Such a model was found to be fully acceptable in the *Suzaku* analysis reported in Itoh et al. (2008), with a reflection fraction (defined as the ratio between the normalizations of the reflector and the intrinsic power-law) of  $3 \times 10^{-3}$ . We simulated various values of  $E_{\text{cut}}$ . Note that  $E_{\text{cut}}$  can be sensitive to calibration uncertainties, especially the cross-normalization between HXI and SGD, so we included a 10% systematic uncertainty in the SGD simulation, as a conservative approximation of our ignorance of such extra uncertainty. Figure 16 shows the result of the constraints on the cutoff when  $E_{\text{cut}} = 400$  keV is assumed for the input spectrum. The figure shows joint confidence intervals for the reflection fraction and  $E_{\text{cut}}$ . It is clear that  $E_{\text{cut}}$  will be significantly constrained despite the degeneracy with the reflection component. If the source happens to be caught in a high flux state with a much harder power-law slope, as in the *Suzaku* observation of Itoh et al. (2008) where  $\Gamma = 1.5 - 1.6$  was measured, the confidence interval on  $E_{\text{cut}}$  will shrink substantially. These improvements over previous data are a consequence of the fact that NGC 4945 is the brightest hard X-ray Sy 2 in the sky, and is thus ideal for SGD observation.

The nucleus of NGC 4945 is the brightest point source in the field above 2 keV. The brightest nearby ULX lies at angular distance of approximately 1 arcmin from the nucleus (Walton et al., 2011) and has an observed 0.2–12 keV luminosity about 10 times lower than the other components (thermal emission and AGN reflection) modeled by Puccetti et al. (2014) in *Suzaku* and *NuSTAR* data. Some other binaries within the central few tens of arcsec contribute at most 50% (combined) of the *Suzaku* flux (Puccetti et al., 2014). But importantly, their spectrum can be represented as simple absorbed power-law ( $\Gamma = 2.2$ ) and they show no evidence of Fe line emission. Therefore, they will not contaminate the detailed analysis of the iron line properties to be carried out with SXS, and simultaneous *Chandra/XMM-Newton* observations are not critical with *ASTRO-H*. A short ( $\sim 10 - 20$  ks), strictly simultaneous *NuSTAR* observation can be considered in order to mitigate the



effect of unknown absolute calibration uncertainties in the early part of the *ASTRO-H* mission. This may prove worthwhile given the strong hard X-ray variability of the source. The *NuSTAR* flux can be used to anchor the HXI flux, thus removing one degree of freedom from the instrumental cross-normalization uncertainties.

## 5 A Space for New Discoveries with *ASTRO-H*

The hard X-ray/soft  $\gamma$ -ray sky is still a poorly explored territory due to limited sensitivities of previous and current instruments operating in this range. On the other hand, non-thermal processes in various types of both transient and steady sources manifest (most) clearly in exactly this domain. In this section some selected topics dealing with non-thermal phenomena in hard X-rays are discussed briefly, to emphasize the space for new discoveries with hard X-ray instruments onboard the *ASTRO-H*.

### 5.1 Tidal Disruption Events

As an example of a source class that may provide surprises as well as crucial information when observed with *ASTRO-H*, we now consider the so-called “tidal disruption events” (TDEs; see Gezari et al., 2009; Saxton & Komossa, 2012, for recent reviews). Two of the observational “clues” often referred to in current scenarios for how and when supermassive black holes grow and possibly interact with their host galaxies are (i) the amounts of AGN (black hole accretion) activity and star formation activity in the Universe appear to evolve in the same manner as a function of time, and (ii) today there appears to be a correlation, the  $M - \sigma$  relation, between the central velocity dispersion of a massive galaxy and the mass of supermassive black hole that always seems to be found at its center. While we can come up with plausible models and even computer simulations for supermassive black hole evolution that are consistent with these clues, the bottom line remains that we still cannot deal confidently with the relevant physics. Moreover, the clues themselves may not be quite right: we may still be missing significant star formation and black hole activity due to obscuration, black hole growth can be intrinsically dark (due to low radiative efficiency or the importance of black hole-black hole mergers), and the  $M - \sigma$  relation shows significant scatter and is based on a relatively small sample of systems. For these reasons, an accurate, theorist-independent, census of supermassive black holes and their activity (“black hole demographics”) is still a holy grail, especially now that we realize that supermassive black holes can release enough energy to radically alter their surroundings (“feedback”). Cutting through obscuration using hard X-ray observations or measuring black hole mass and spin by constraining the size of the innermost stable orbit via lower energy X-ray observations, e.g., by the SXS, are discussed extensively in the “AGN Reflection” *ASTRO-H* White Paper. None of these approaches help, however, if the supermassive black hole is simply shut off, i.e., not accreting or radiating strongly – which is actually the case most of the time given the rarity of AGN activity, especially at redshifts  $z < 1$ .

Tidal disruption events, once properly understood, offer a potentially powerful way to make progress on the black hole demographics problem. Even if a supermassive black hole, like the one at the center of our galaxy, is presently starved of gas, there is a non-zero chance that a star orbiting in the host galaxy nucleus will get scattered onto an orbit that takes it very close to the black hole. If the star gets close enough (crossing the tidal disruption radius), the tidal force on the star due to the black hole’s gravity overwhelms the self-gravity of the star, shredding it and sending a significant fraction of its mass into the black hole on a timescale of months according to current estimates. Since a mass accretion rate  $\sim 1 M_{\odot} \text{yr}^{-1}$  corresponds to that of a powerful quasar, a tidal disruption event should be a fairly obvious and unambiguous signature of the presence of a supermassive black hole – if we happen to be looking at the right time. Unfortunately, while tidal disruption effects may be dramatic, they are also rare. The rate at which stars scatter into the black hole depends sensitively on the dynamical state of the host galaxy nucleus, but it is estimated to 1 per  $10^4$  to  $10^6$  years (Merritt & Wang, 2005; Vasiliev & Merritt, 2013). In other words, if we hope to see one disruption event in a year, we need to monitor at least one million galaxies on at least  $\sim$  month timescales. This is still a tall order, indeed an impossible one for a narrow field-of-view instrument like *ASTRO-H*, but it is one that is becoming increasingly feasible given the advent of increasingly sensitive large-area surveys. Already the reports of TDE candidates

are a few per year, and the arrival of LSST at the tail end of the *ASTRO-H* mission could boost that rate to  $\gtrsim 100$  per year if our current understanding of TDEs is correct.

While *ASTRO-H* may not be able to find TDEs, it can play a key role in confirming that a candidate event is a TDE and then helping to unravel the astrophysics of the event using its broadband suite of instruments. As evidenced by the long debate over the starburst vs. black hole origin of AGN activity, the fact that supernova searches studiously avoid the centers of galaxies, and that luminous blue variable stars like Eta Carinae instead tend to be found near centers of galaxies and can flare by many magnitudes on the timescale of years, it is actually quite easy to confuse processes related to stars with those arising from black holes. The arguments usually end, however, with the detection of intense hard X-ray ( $> 10$  keV) flux that also varies rapidly on  $\sim$  hour to day timescales. As the most sensitive hard X-ray telescopes operating, *NuSTAR* and *ASTRO-H* therefore have an important role to play. Indeed Figure 17 shows two recent (and unexpected!) examples of TDE candidates where hard X-ray measurements played a key role in arguing for a supermassive black hole origin of the emission. The event SWIFT 1644+57, in fact, was originally discovered as a gamma-ray burst (which then refused to fade, see Levan et al., 2011; Bloom et al., 2011, for more discussion of this source). For that object, not only would *ASTRO-H* have seen a strong signal in all instruments, allowing it to measure and track the shape of the high-energy spectrum much better than *Swift* (particularly at energies above 100 keV, where a cutoff might start becoming visible), but for the first few days, the source was so bright ( $\sim 10^{-9}$  erg cm $^{-2}$  s $^{-1}$ ) that SGD would either measure or strongly constrain the polarization of the high-energy flux, in turn placing important constraints on the physical emission mechanism. Given that supermassive black holes are known to produce powerful relativistic jets, in retrospect the detection of a TDE at  $\sim$  MeV energies might not be so surprising, despite the standard prediction for TDE events that their emission peaks at the energies typical of an optically thick AGN accretion disk, at UV to soft X-ray energies. Even if most TDEs follow the standard prediction, essentially every black hole system we know of has coronal X-ray emission that also excites atomic features such as iron fluorescence lines. Given that within 100 Mpc of us, there are over 50,000 known galaxies and probably more unknown that have not had their redshifts measured yet, the odds of having a bright, nearby TDE occur during the *ASTRO-H* are not small. In this case, prompt and repeated observations by *ASTRO-H*'s instrument suite, including the SXS, can uniquely help us track and probe the response and evolution of the inner accretion flow through a large change in mass accretion rate. Not only may TDEs turn out to be key probes of black hole demographics, but well-observed TDEs may also represent some of the best laboratories to probe AGN accretion physics. The analogs of state transitions in stellar mass black holes, if they occur at all for AGN, would take ten of thousands to millions of years if we simply scaled by mass from the  $\sim$  month-year timescales for stellar mass black holes. In the case of a TDE, however, a star on a plunging orbit that then disrupts close to the black hole can deliver gas much faster to the black hole, circumventing the need for gas to move (slowly) through the outer parts of the accretion disk.

## 5.2 High-redshift Blazars

The discovery of bright (mostly radio-quiet) quasars at the redshifts  $z \sim 6$  and beyond (Fan et al., 2006; Willott et al., 2010; Mortlock et al., 2011) implies that SMBHs with masses  $\geq 10^9 M_{\odot}$  were already assembled and fully developed when the Universe was less than 1 Gyr-old. The mechanism by which such systems formed during the first Gyr after the Big Bang is currently debated. In addition to this, the all-sky *Swift*-BAT survey identified about 10 luminous blazars at redshifts greater than 2. Although accessing the energetics of jets (as well as black hole masses) in blazar sources is rather model-dependent, the high- $z$  blazars detected by BAT seem to be particularly powerful and produced by particularly massive black holes accreting at Eddington rates (Ghisellini et al., 2011, 2013). Importantly, the number of such objects can be used to constrain the parent population of jetted AGN in the early Universe in general. As discussed in Volonteri et al. (2011), a comparison between the high- $z$  blazar sample and quasars detected in the Sloan Digital Sky Survey (SDSS), indicates a serious deficit of ‘misaligned’ radio-loud AGN at  $z > 3$ . Possible explanations for this disagreement elaborated in Volonteri et al. include lower bulk Lorentz factors of high-redshift quasar jets when compared with their low-redshift analogs, or the incompleteness of the utilized SDSS sample. *ASTRO-H* can contribute to the study of high- $z$  blazars by

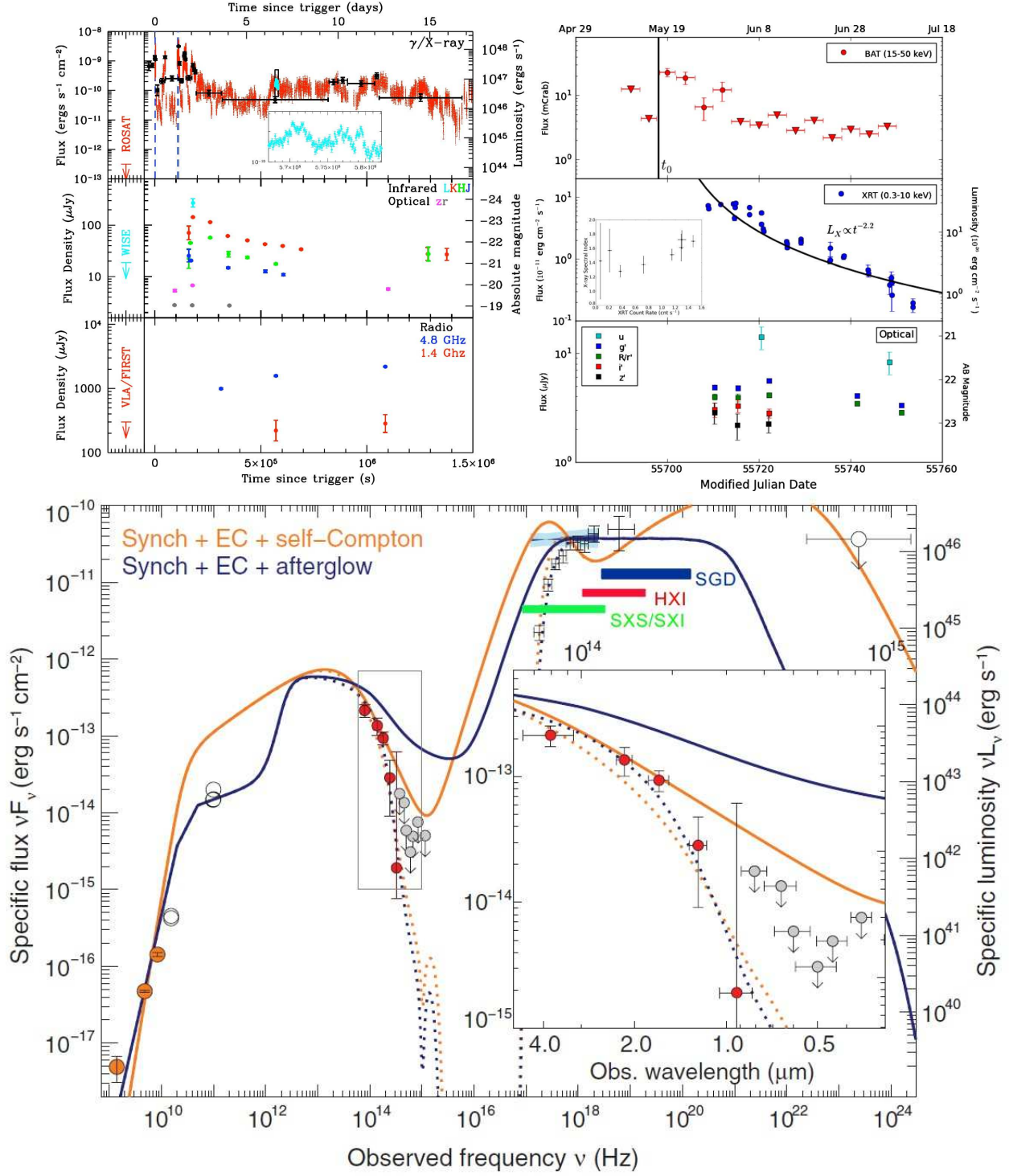


**Figure 17:** Upper left panel: Light curves at multiple energies for the unusual TDE candidate, SWIFT 1644+57 (Levan et al., 2011). Note the high flux at hard X-ray energies, particularly at the beginning of the burst. Lower panel: A snapshot of the spectral energy distribution of SWIFT 1644+57 and possible emission models to explain it, adapted from Bloom et al. (2011). The broad energy coverage provided by the *ASTRO-H* instruments (shown by the red, green, and blue horizontal bars) would play an important role in constraining possible emission mechanisms, particularly by measuring or placing lower limits on the cutoff energy of the high-energy peak. Upper right panel: Light curves, adapted from Cenko et al. (2012), for another “high-energy” TDE candidate, SWIFT 2058+05, that appears similar to SWIFT 1644+57. This event was found not long after SWIFT 1644+57, indicating that events of this type may actually not be that rare.

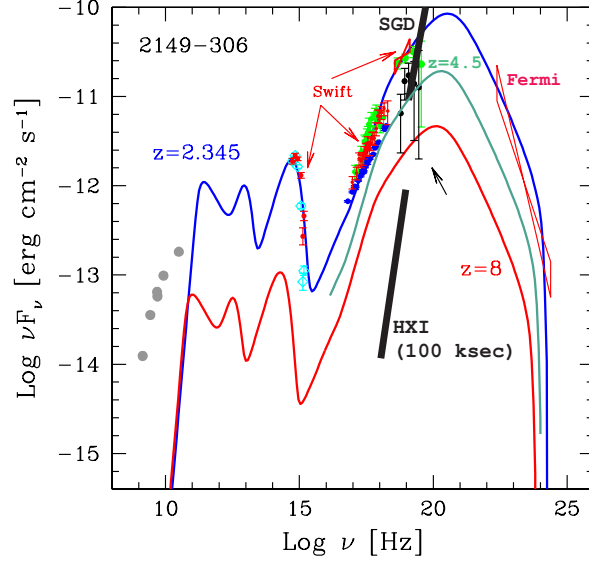


**Figure 18:** Broad-band spectral energy distribution of the  $z = 2.345$  blazar 2149–306, along with the spectral model fit (blue curve) adopted from Ghisellini et al. (2010). In addition, the green and red curves illustrate the source spectrum shifted to the redshifts  $z = 4.5$  and 8, respectively. The HXI and SGD sensitivity curves corresponding to the 100 ks exposure are shown as thick black lines.

means of a detailed spectral characterization of their broad-band X-ray continua, allowing for a precise insight into the source energetics (see Figure 18; see also in this context Sbarrato et al., 2013, for the recent *NuSTAR* results). It is important to note here that the majority of the discussed objects release the bulk of their radiative power at MeV frequencies, and as such are particularly luminous in hard X-rays; moreover, luminous blazars are often characterized by flat or very flat hard X-ray spectra (photon indices  $\Gamma < 2$ , see Sikora et al., 2009).

### 5.3 Non-thermal Emission of Novae

A nova eruption is a thermonuclear runaway on the surface of a white dwarf that ejects much of the hydrogen-rich envelope that the star has accreted. Many novae have been detected in the 0.5–10 keV band as sources of optically-thin, collisionally-excited thermal plasma emission (Mukai et al., 2008). This indicates that shocks are ubiquitous in novae. The recent discovery of GeV emission first from V407 Cyg (Abdo et al., 2010a) and subsequently several others with *Fermi*-LAT indicates that nova shocks are also capable of particle acceleration. In addition, the detection of apparent synchrotron emission in the radio (see, e.g., Rupen et al., 2014) in some novae is further evidence for a population of accelerated electrons. We will gain a better understanding of the accelerated particles in nova shocks if we can detect and characterize the associated hard X-rays. This has so far only been claimed in one nova, V2491 Cyg (Takei et al., 2009), using non-imaging *Suzaku* HXD/PIN data, but this erupted shortly before the launch of *Fermi*, so there is no constraint on its GeV emission. If a sufficiently bright nova is discovered during the *ASTRO-H* era, particularly one that is detected with *Fermi*-LAT, it will be an excellent target for *ASTRO-H* HXI observation for this possible non-thermal hard X-ray component, while the SXS will be able to provide an in-depth characterization of the thermal X-ray emission.

### 5.4 Unidentified Hard X-ray/soft $\gamma$ -ray Sources

COMPTEL instrument onboard the CGRO provided the first complete all-sky survey in the energy range 0.75 to 30 MeV. The First COMPTEL Catalogue includes 32 steady sources and about 50 transients; among the continuum sources are spin-down pulsars, XRBs, supernova remnants, interstellar clouds, AGN, gamma-ray bursts, and solar flares (Schönfelder et al., 2000). The third IBIS/ISGRI catalog, based on  $> 40$  Ms observations performed during 3.5 yrs of the *INTEGRAL* operation, includes  $> 400$  sources detected in the 17–100 keV range (Bird et al., 2007). Finally, the *Swift*-BAT 70-month survey has detected 1171 hard X-ray sources in the 14–

195 keV band down to a significance level of  $4.8\sigma$ , associated with 1210 counterparts including various types of AGN, clusters, cataclysmic variables, pulsars, stars, supernova remnants, and XRBs (Baumgartner et al., 2013). Thus, the hard X-ray/soft  $\gamma$ -ray sky is crowded indeed, being populated by a variety of high-energy emitters. Among these, some sources still remain to be identified, and many to be characterized precisely (regarding their spectral and timing properties) at  $> 10$  keV photon energies. This constitutes a space for potential new exciting discoveries with the high-energy instruments HXI and SGD onboard the *ASTRO-H* in the near future.

## References

- Abdo, A. A., Ackermann, M., Ajello, M., et al. 2010a, *Science*, 329, 817
- Abdo, A. A., Ackermann, M., Ajello, M., et al. 2010b, *Nature*, 463, 919
- Abdo, A. A., Ackermann, M., Ajello, M., et al. 2010c, *ApJL*, 714, L73
- Abdo, A. A., Ackermann, M., Ajello, M., et al. 2010d, *ApJ*, 719, 1433
- Abdo, A. A., Ackermann, M., Ajello, M., et al. 2011a, *ApJ*, 727, 129
- Abdo, A. A., Ackermann, M., Ajello, M., et al. 2011b, *ApJ*, 736, 131
- Ackermann, M., Ajello, M., Allafort, A., et al. 2012, *ApJ*, 755, 164
- Aharonian, F., Akhperjanian, A. G., Bazer-Bachi, A. R., et al. 2007, *ApJL*, 664, L71
- Aharonian, F., Akhperjanian, A. G., Anton, G., et al. 2009, *ApJL*, 695, L40
- Arévalo, P., Bauer, F. E., Puccetti, S., et al. 2014, *ApJ*, 791, 81
- Asmus, D., Hönig, S. F., Gandhi, P., Smette, A., & Duschl, W. J. 2014, *MNRAS*, 439, 1648
- Bauer, F. E., Brandt, W. N., Sambruna, R. M., et al. 2001, *AJ*, 122, 182
- Baumgartner, W. H., Tueller, J., Markwardt, C. B., et al. 2013, *ApJS*, 207, 19
- Beckmann, V., Jean, P., Lubiński, P., et al. 2011, *A&A*, 531, 70
- Begelman, M. C., & Sikora, M. 1987, *ApJ*, 322, 650
- Begelman, M. C., Blandford, R. D., & Rees, M. J. 1984, *Reviews of Modern Physics*, 56, 255
- Beilicke, M., Baring, M. G., Barthelmy, S., et al. 2012, *American Institute of Physics Conference Series*, 1505, 805
- Bellazzini, R., Costa, E., Matt, G., & Tagliaferri, G. 2010, *X-ray Polarimetry: A New Window in Astrophysics* by Ronaldo Bellazzini, Enrico Costa, Giorgio Matt and Gianpiero Tagliaferri. Cambridge University Press, 2010
- Bird, A. J., Malizia, A., Bazzano, A., et al. 2007, *ApJS*, 170, 175
- Black, J. K., Deines-Jones, P., Hill, J. E., et al. 2010, *Space Telescopes and Instrumentation*, 7732,
- Blandford, R., Agol, E., Broderick, A., et al. 2002, *Astrophysical Spectropolarimetry*, 177
- Bloom, J. S., Giannios, D., Metzger, B. D., et al. 2011, *Science*, 333, 203
- Bloser, P. F., Legere, J. S., McConnell, M. L., et al. 2009, *Nuclear Instruments and Methods in Physics Research A*, 600, 424
- Bonometto, S., & Saggion, A. 1973, *A&A*, 23, 9
- Celotti, A., & Matt, G. 1994, *MNRAS*, 268, 451
- Cenko, S. B., Krimm, H. A., Horesh, A., et al. 2012, *ApJ*, 753, 77
- Chatterjee, R., Marscher, A. P., Jorstad, S. G., et al. 2009, *ApJ*, 704, 1689
- Chatterjee, R., Marscher, A. P., Jorstad, S. G., et al. 2011, *ApJ*, 734, 43
- Chernyakova, M., Neronov, A., Courvoisier, T. J.-L., et al. 2007, *A&A*, 465, 147
- Collins, P., Kyne, G., Lara, D., et al. 2013, *Experimental Astronomy*, 36, 479
- Costa, E., Bellazzini, R., Tagliaferri, G., et al. 2010, *Experimental Astronomy*, 28, 137
- Courvoisier, T. J.-L. 1998, *A&ARv*, 9, 1
- Courvoisier, T. J.-L., Beckmann, V., Bourban, G., et al. 2003, *A&A*, 411, L343
- Dean, A. J., Clark, D. J., Stephen, J. B., et al. 2008, *Science*, 321, 1183
- Done, C., Madejski, G. M., & Smith, D. A. 1996, *ApJL*, 463, L63
- Droulans, R., & Jourdain, E. 2009, *A&A*, 494, 229
- Elmouttie, M., Haynes, R. F., Jones, K. L., et al. 1997, *MNRAS*, 284, 830
- Evans, D. A., Kraft, R. P., Worrall, D. M., et al. 2004, *ApJ*, 612, 786
- Fan, X., Strauss, M. A., Richards, G. T., et al. 2006, *AJ*, 131, 1203
- Fender, R. P., Homan, J., & Belloni, T. M. 2009, *MNRAS*, 396, 1370
- Forot, M., Laurent, P., Grenier, I. A., Gouiffès, C., & Lebrun, F. 2008, *ApJL*, 688, L29
- Fukazawa, Y., Hiragi, K., Mizuno, M., et al. 2011a, *ApJ*, 727, 19

- Fukazawa, Y., Hiragi, K., Yamazaki, S., et al. 2011b, *ApJ*, 743, 124
- Fukazawa, Y., Finke, J., Stawarz, Ł., et al. 2014, *ApJ*, in press (arXiv:1410.2733)
- Gandhi, P., Yamada, S., Ricci, C., et al. 2014, *MNRAS*, submitted (arXiv:1408.4453)
- Gezari, S., Strubbe, L., Bloom, J. S., et al. 2009, *astro2010: The Astronomy and Astrophysics Decadal Survey*, 2010, 88
- Ghisellini, G., Della Ceca, R., Volonteri, M., et al. 2010, *MNRAS*, 405, 387
- Ghisellini, G., Tagliaferri, G., Foschini, L., et al. 2011, *MNRAS*, 411, 901
- Ghisellini, G., Nardini, M., Tagliaferri, G., J., et al. 2013, *MNRAS*, 428, 1449
- Gofford, J., Reeves, J. N., Tombesi, F., et al. 2013, *MNRAS*, 430, 60
- Goulding, A. D., & Alexander, D. M. 2009, *MNRAS*, 398, 1165
- Götz, D., Laurent, P., Lebrun, F., Daigne, F., & Bošnjak, Ž. 2009, *ApJL*, 695, L208
- Greenhill, L. J., Moran, J. M., & Herrnstein, J. R. 1997, *ApJL*, 481, L23
- Hartman, R. C., Bertsch, D. L., Bloom, S. D., et al. 1999, *ApJS*, 123, 79
- Hayashida, M., Stawarz, Ł., Cheung, C. C., et al. 2013, *ApJ*, 779, 131
- Hester, J. J., Scowen, P. A., Sankrit, R., et al. 1995, *ApJ*, 448, 240
- Hill, J. E., McConnell, M. L., Bloser, P., et al. 2008, *American Institute of Physics Conference Series*, 1065, 331
- Hönig, S. F., Kishimoto, M., Tristram, K. R. W., et al. 2013, *ApJ*, 771, 87
- Israel, F. P. 1998, *A&ARv*, 8, 237
- Itoh, T., Done, C., Makishima, K., et al. 2008, *PASJ*, 60, 251
- Iwasawa, K., Koyama, K., Awaki, H., et al. 1993, *ApJ*, 409, 155
- Johnson, W. N., Dermer, C. D., Kinzer, R. L., et al. 1995, *ApJ*, 445, 182
- Jourdain, E., Roques, J. P., Chauvin, M., & Clark, D. J. 2012, *ApJ*, 761, 27
- Kataoka, J., Tanihata, C., Kawai, N., et al. 2002, *MNRAS*, 336, 932
- Kataoka, J., Stawarz, Ł., Takahashi, Y., et al. 2011, *ApJ*, 740, 29
- Kormendy, J., & Ho, L. C. 2013, *ARA&A*, 51, 511
- Krabbe, A., Böker, T., & Maiolino, R. 2001, *ApJ*, 557, 626
- Krawczynski, H. 2012, *ApJ*, 744, 30
- Krawczynski, H., Garson, A., Guo, Q., et al. 2011, *Astroparticle Physics*, 34, 550
- Laurent, P., Rodriguez, J., Wilms, J., et al. 2011, *Science*, 332, 438
- Lei, F., Dean, A. J., & Hills, G. L. 1997, *Space Science Reviews*, 82, 309
- Lenc, E., & Tingay, S. J. 2009, *AJ*, 137, 537
- Levan, A. J., Tanvir, N. R., Cenko, S. B., et al. 2011, *Science*, 333, 199
- Liedahl, D. A., & Paerels, F. 1996, *ApJL*, 468, L33
- Lightman, A. P., & Shapiro, S. L. 1976, *ApJ*, 203, 701
- Lohfink, A. M., Reynolds, C. S., Jorstad, S. G., et al. 2013, *ApJ*, 772, 83
- Long, K. S., Chanan, G. A., & Novick, R. 1980, *ApJ*, 238, 710
- Maccione, L., Liberati, S., Celotti, A., Kirk, J. G., & Ubertini, P. 2008, *Phys.Rev.D*, 78, 103003
- Madejski, G., Życki, P., Done, C., et al. 2000, *ApJL*, 535, L87
- Marconi, A., Oliva, E., van der Werf, P. P., et al. 2000, *A&A*, 357, 24
- Markowitz, A., Takahashi, T., Watanabe, S., et al. 2007, *ApJ*, 665, 209
- Marinucci, A., Risaliti, G., Wang, J., et al. 2012, *MNRAS*, 423, L6
- Marscher, A. P., Jorstad, S. G., Gómez, J.-L., et al. 2002, *Nature*, 417, 625
- Marscher, A. P., Jorstad, S. G., D’Arcangelo, F. D., et al. 2008, *Nature*, 452, 966
- Massaro, F., Bianchi, S., Matt, G., D’Onofrio, E., & Nicastro, F. 2006, *A&A*, 455, 153
- Mayer, M., Buehler, R., Hays, E., et al. 2013, *ApJL*, 775, L37
- McGlynn, S., Clark, D. J., Dean, A. J., et al. 2007, *A&A*, 466, 895
- McKinney, J. C. 2006, *MNRAS*, 368, 1561
- McNamara, A. L., Kuncic, Z., & Wu, K. 2009, *MNRAS*, 395, 1507
- Merritt, D., & Wang, J. 2005, *ApJL*, 621, 101
- Mirabel, I. F., & Rodríguez, L. F. 1994, *Nature*, 371, 46
- Moorwood, A. F. M., & Oliva, E. 1994, *ApJ*, 429, 602
- Moorwood, A. F. M., van der Werf, P. P., Kotilainen, J. K., Marconi, A., & Oliva, E. 1996, *A&A*, 308, L1
- Moran, P., et al., 2013, arXiv:1302.3622v1
- Mortlock, D. J., Warren, S. J., Venemans, B. P., et al. 2011, *Nature*, 474, 616

- Mukai, K., Orio, M., & Della Valle, M. 2008, *ApJ*, 677, 1248
- Murphy, K. D., & Yaqoob, T. 2009, *MNRAS*, 397, 1549
- Odaka, H., et al., 2010, *Nucl. Instr. Meth. A*, 624, 303
- Orsi, S., & Polar Collaboration 2011, *Astrophysics and Space Sciences Transactions*, 7, 43
- Ozaki, M., et al., 2012, *Proc. SPIE*, 8443, 844356
- Pacholczyk A. G., Swihart T. L., 1967, *ApJ*, 150, 647
- Pearce, M., Florén, H.-G., Jackson, M., et al. 2012, *arXiv:1211.5094*
- Pian, E., Vacanti, G., Tagliaferri, G., et al. 1998, *ApJL*, 492, L17
- Porquet, D., & Dubau, J. 2000, *A&AS*, 143, 495
- Poutanen, J. 1994, *ApJS*, 92, 607
- Puccetti, S., Comastri, A., Fiore, F., et al. 2014, *ApJ*, 793, 26
- Rodriguez, J., Shaw, S. E., Hannikainen, D. C., et al. 2008, *ApJ*, 675, 1449
- Rupen, M. P., Mioduszewski, A. J., Chomiuk, L., et al. 2014, *The Astronomer's Telegram*, 5884, 1
- Sambruna, R. M., Brandt, W. N., Chartas, G., et al. 2001a, *ApJL*, 546, L9
- Sambruna, R. M., Netzer, H., Kaspi, S., et al. 2001b, *ApJL*, 546, L13
- Saxton, R., & Komossa, S. 2012, *European Physical Journal Web of Conferences*, 39, 00001
- Sądowski, A., Narayan, R., McKinney, J. C., & Tchekhovskoy, A. 2014, *MNRAS*, 439, 503
- Sbarrato, T., Tagliaferri, G., Ghisellini, G., et al. 2013, *ApJ*, 777, 147
- Schönfelder, V., Bennett, K., Blom, J. J., et al. 2000, *A&AS*, 143, 145
- Schurch, N. J., Roberts, T. P., & Warwick, R. S. 2002, *MNRAS*, 335, 241
- Shu, X. W., Yaqoob, T., & Wang, J. X. 2011, *ApJ*, 738, 147
- Sikora, M., Stawarz, Ł., Moderski, R., Nalewajko, K., & Madejski, G. M. 2009, *ApJ*, 704, 38
- Słowikowska, A., Kanbach, G., Kramer, M., & Stefanescu, A. 2009, *MNRAS*, 397, 103
- Smith, F. G., Jones, D. H. P., Dick, J. S. B., & Pike, C. D. 1988, *MNRAS*, 233, 305
- Soffitta, P., Barcons, X., Bellazzini, R., et al. 2013, *Experimental Astronomy*, 36, 523
- Soldi, S., Türler, M., Paltani, S., et al. 2008, *A&A*, 486, 411
- Steinle, H., Bennett, K., Bloemen, H., et al. 1998, *A&A*, 330, 97
- Stirling, A. M., Spencer, R. E., de la Force, C. J., et al. 2001, *MNRAS*, 327, 1273
- Striani, E., Tavani, M., Piano, G., et al. 2011, *ApJL*, 741, L5
- Tajima, H. et al., 2010, *Proc. SPIE*, 7732, 773216
- Tajima, H. et al., 2010, *X-ray Polarimetry: A New Window in Astrophysics* by Cambridge University Press, p. 275
- Takahashi, T., Uchiyama, Y., & Stawarz, Ł. 2013, *Astroparticle Physics*, 43, 142
- Takeda, S., et al., 2010, *Nucl. Instr. Meth. A*, 622, 619
- Takei, D., Tsujimoto, M., Kitamoto, S., et al. 2009, *ApJL*, 697, L54
- Tavani, M., Bulgarelli, A., Vittorini, V., et al. 2011, *Science*, 331, 736
- Tchekhovskoy, A., Narayan, R., & McKinney, J. C. 2011, *MNRAS*, 418, L79
- Tombesi, F., Sambruna, R. M., Reeves, J. N., et al. 2010a, *ApJ*, 719, 700
- Tombesi, F., Cappi, M., Reeves, J. N., et al. 2010b, *A&A*, 521, A57
- Tombesi, F., Sambruna, R. M., Marscher, A. P., et al. 2012, *MNRAS*, 424, 754
- Tombesi, F., Reeves, J. N., Reynolds, C. S., García, J., & Lohfink, A. 2013, *MNRAS*, 434, 2707
- Tombesi, F., Tazaki, Mushotzky, R. F., Ueda, Y., et al. 2014, *MNRAS*, 443, 2154
- Reeves, J. N., Gofford, J., Braitto, V., & Sambruna, R. 2010, *ApJ*, 725, 803
- Urry, C. M., & Padovani, P. 1995, *PASP*, 107, 803
- Vasiliev, E., & Merritt, D. 2013, *ApJ*, 774, 87
- Vasudevan, R. V., Fabian, A. C., Gandhi, P., Winter, L. M., & Mushotzky, R. F. 2010, *MNRAS*, 402, 1081
- Volonteri, M., Haardt, F., Ghisellini, G., & Della Ceca, R. 2011, *MNRAS*, 416, 216
- Walton, D. J., Roberts, T. P., Mateos, S., & Heard, V. 2011, *MNRAS*, 416, 1844
- Watanabe, S., et al., 2012, *Proc. SPIE*, 8443, 844326
- Watanabe, S., et al., 2014, *Nucl. Instr. Meth. A*, in press
- Weisskopf, M. C., Cohen, G. G., Kestenbaum, H. L., et al. 1976, *ApJL*, 208, L125
- Weisskopf, M. C., Elsner, R. F., Kaspi, V. M., et al. 2009, *Astrophysics and Space Science Library*, 357, 589
- Willott, C. J., Delorme, P., Reylé, C., et al. 2010, *AJ*, 139, 906
- Yang, Y., Wilson, A. S., Matt, G., Terashima, Y., & Greenhill, L. J. 2009, *ApJ*, 691, 131
- Yaqoob, T. 2012, *MNRAS*, 423, 3360
- Zdziarski, A. A., Pjanka, P., Sikora, M., & Stawarz, Ł. 2014, 442, 3243
- Zhang, H., Boettcher, M. 2013, *ApJ*, 774, 18